



Deposited via The University of York.

White Rose Research Online URL for this paper:

<https://eprints.whiterose.ac.uk/id/eprint/215349/>

Version: Other

Preprint:

Stephen, Nicholas, Pinto-Huguet, Ivan, Lawrence, Robert et al. (2024) Evaluating the local bandgap across InxGa1-xAs multiple quantum wells in a metamorphic laser via low-loss EELS. [Preprint]

<https://doi.org/10.48550/arXiv.2406.06816>

Reuse

Items deposited in White Rose Research Online are protected by copyright, with all rights reserved unless indicated otherwise. They may be downloaded and/or printed for private study, or other acts as permitted by national copyright laws. The publisher or other rights holders may allow further reproduction and re-use of the full text version. This is indicated by the licence information on the White Rose Research Online record for the item.

Takedown

If you consider content in White Rose Research Online to be in breach of UK law, please notify us by emailing eprints@whiterose.ac.uk including the URL of the record and the reason for the withdrawal request.

Evaluating the local bandgap across $\text{In}_x\text{Ga}_{1-x}\text{As}$ multiple quantum wells in a metamorphic laser via low-loss EELS

Nicholas Stephen^{*1}, Ivan Pinto-Huguet², Robert Lawrence³, Demie Kepaptsoglou^{3,4}, Marc Botifoll², Agnieszka Gocalinska⁵, Enrica Mura⁵, Emanuele Pelucchi⁵, Jordi Arbiol^{2,6} and Miryam Arredondo^{1*}

¹ School of Mathematics and Physics, Queen's University Belfast, University Road, Belfast, UK.

² Catalan Institute of Nanoscience and Nanotechnology (ICN2), CISC and BIST, Campus UAB, Bellaterra, 08193 Barcelona, Catalonia, Spain.

³ School of Physics, Engineering and Technology, University of York, Heslington, York, UK.

⁴ SuperSTEM Laboratory, SciTech Daresbury Campus, Daresbury, UK.

⁵ Tyndall National Institute, University College Cork, "Lee Maltings", Dyke Parade, Cork, Ireland.

⁶ ICREA, Pg. Lluis Companys 23, 08010 Barcelona, Catalonia, Spain.

*nstephen01@qub.ac.uk, *m.arredondo@qub.ac.uk

Keywords: Electron Energy Loss Spectroscopy, Bandgap, Quantum Well, InGaAs, In concentration, Strain.

Abstract

We investigate spatially resolved variations in the bandgap energy across multiple $\text{In}_x\text{Ga}_{1-x}\text{As}$ quantum wells (QWs) on a GaAs substrate within a metamorphic laser structure. Using high resolution scanning transmission electron microscopy and low-loss electron energy loss spectroscopy, we present a detailed analysis of the local bandgap energy, indium concentration, and strain distribution within the QWs. Our findings reveal significant inhomogeneities, particularly near the interfaces, in both the strain and indium content, and a bandgap variability across QWs. These results are correlated with density functional theory simulations to further elucidate the interplay between strain, composition, and bandgap energy. This work underscores the importance of spatially resolved analysis in understanding, and optimising, the electronic and optical properties of semiconductor devices. The study suggests that the collective impact of individual QWs might affect the emission and performance of the final device, providing insights for the design of next-generation metamorphic lasers with multiple QWs as the active region.

Introduction

The integration of metamorphic buffers (MB) into laser structures has significantly advanced the design and fabrication of semiconductor devices, especially for telecommunication applications. By incorporating a buffer layer between the substrate and the active region, metamorphic lasers mitigate lattice constant mismatches, enabling the development and fabrication of novel $\text{In}_x\text{Ga}_{1-x}\text{As}$ structures (where x is mole fraction). These structures, such as quantum wells (QWs)/GaAs lasers, have been shown to enhance and tailor the optoelectronic properties of semiconductor lasers [1–5]. Multiple QWs (MQWs) offer several advantages over using single QWs, including reduced threshold current

[6], decreased sensitivity to temperature variations [7] and improved quantum efficiency [8]. Moreover, adjusting the thickness [9, 10] and number of QWs [11] allows tuning of the emission wavelength due to carriers interactions within the laser [12, 13], thus enhancing the overall laser performance (under specific assumptions in terms of homogeneity).

Central to the performance of semiconductor lasers is the bandgap energy (E_g), a fundamental property governing optical transitions. Management and engineering of the E_g is essential in designing various laser applications. $\text{In}_x\text{Ga}_{1-x}\text{As}$ has a direct E_g which is intrinsically linked to the Indium (In) concentration, playing a key role in tuning laser emissions to wavelengths ranging from 1300nm to 1550nm, predominantly used in telecommunication applications [1, 5, 14]. Additionally, the In concentration directly influences the lattice constant [15], which in turn determines the type and magnitude of strain within the layers. Both compressive and tensile strain can significantly alter the E_g value by modifying the energy levels of the orbitals, an effect well documented in various works [16–22]. In fact, strain engineering or strain management is commonly used as an approach to varying the E_g . Thus, understanding the interplay between composition, strain and E_g is essential for the design of the next-generation metamorphic lasers.

Traditionally, a variety of techniques are used to measure the E_g including UV-Vis spectroscopy [23], X-ray photoelectron spectroscopy [24] and photoluminescence [25]. While effective for bulk materials, these techniques are often limited by spatial resolution. Studies at the nanoscale can reveal physical phenomena that are not apparent at larger scales especially given the potential heterogeneity in composition, strain, and defects within the thin film, which can create localised states within E_g . Low-loss electron energy loss spectroscopy (EELS) [26, 27] offers a significant advantage by probing the capability to probe the electronic structure at high spatial resolution with comparable energy resolution to traditional techniques [28, 29], making it the ideal tool for measuring the E_g at the nanoscale [30]. This technique has been applied to various semiconductor materials including Cu(In,Ga)Se solar cells [31], CdSe quantum dots (QDs) [26], alpha-alumina grain boundaries [32], WS_2 nanoflowers [33] and $\text{Mo}_x\text{W}_{1-x}\text{S}_2$ nanoflakes [34]. While low-loss EELS has been used in $\text{In}_x\text{Ga}_{1-x}\text{As}$ structures to measure the E_g in QDs [35] and nanowires [36], to the authors knowledge, spatially resolved E_g measurements in multiple $\text{In}_x\text{Ga}_{1-x}\text{As}$ QWs, integrated in a device architecture such as metamorphic lasers, remains unexplored.

This study employs low-loss EELS to investigate spatial variations in the E_g across three stacked QWs within an $\text{In}_{0.40}\text{Ga}_{0.60}\text{As}$ QW/GaAs metamorphic laser structure. The localised strain and In concentration across individual QWs are also investigated and correlated to the measured E_g values. This work highlights the delicate role that composition and strain play on the E_g of $\text{In}_x\text{Ga}_{1-x}\text{As}$ QWs, contributing towards a better understanding of the nanoscale mechanisms that govern their electronic

and optical properties. These findings provide a deeper understanding of the factors affecting the E_g and how variations across individual QWs may impact the final laser emission.

Results and Discussion

In atomic fraction mapping

Figure 1a displays the high angle annular dark field-scanning transmission electron microscopy (HAADF-STEM) overview of the metamorphic laser structure, a schematic diagram of the full structure is detailed in Fig. S1 in Supplementary information (SI), and elsewhere [37, 38]. The area of interest is that containing the multiple QWs as shown in Fig. 1b. This region consists of a 5nm GaAs interface controlling layer (CIL), a 7nm $\text{In}_{0.40}\text{Ga}_{0.60}\text{As}$ QW followed by a 20nm $\text{In}_{0.13}\text{Ga}_{0.87}\text{As}$ barrier (all nominal thickness), repeated three times. For clarity, the QW here referred as the bottom QW is that nearest to the $\text{In}_x\text{Ga}_{1-x}\text{As}$ MB, while the top QW is that furthest away from MB. The measured thickness of all QWs is $\sim 8.6\text{nm}$ (Table S1), with some visible roughness at the interfaces (Fig. 1b).

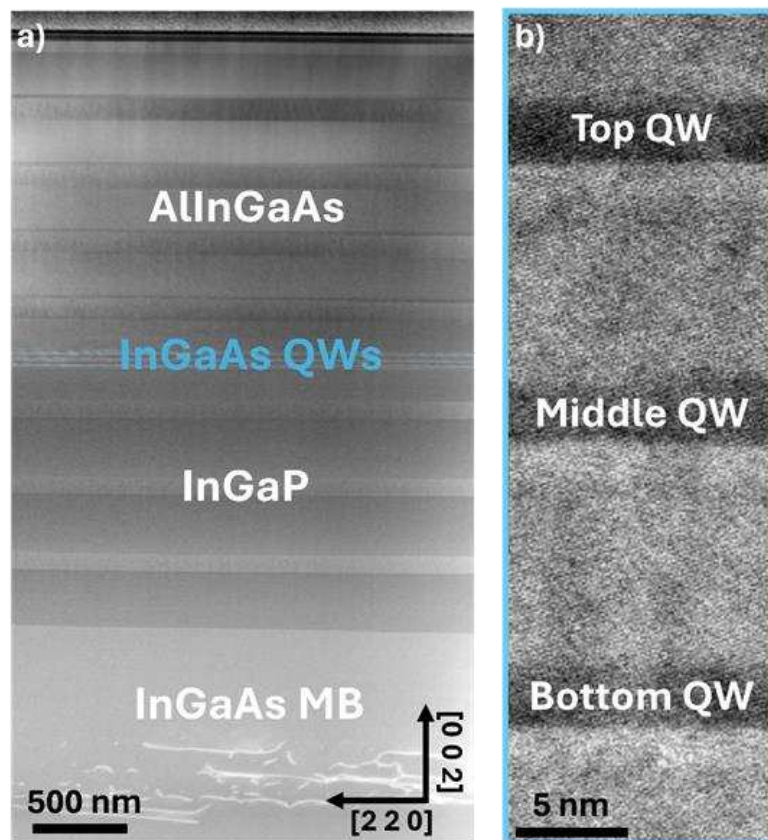


Figure 1. HAADF-STEM overview (a) and the $\text{In}_{0.40}\text{Ga}_{0.60}\text{As}$ QWs region (b).

The E_g is significantly influenced by both In concentration and strain [16–20, 39, 40]. The relationship between In concentration and the resulting E_g is well established. Previous reports by Goetz *et al.* [39] and Fleischmann *et al.* [40] have demonstrated that increasing the In concentration

increases the emission wavelength, thereby decreasing the E_g . For QWs, the E_g is also intrinsically linked to the dimensions of the confinement, if confined. Any variations in the composition or thickness of a material such as $\text{In}_x\text{Ga}_{1-x}\text{As}$ will lead to changes in the band structure, consequently affecting its E_g .

Figure 2 displays the In atomic fraction (at. %) maps across all QWs, highlighting a clear inhomogeneous distribution of In (particularly near the interfaces) which varies between individual QWs. For clarity, $\text{In}_{0.40}\text{Ga}_{0.60}\text{As}$ QW, here expressed in mole fraction, indicates that 50% of the atoms are As, 30% are Ga and the remaining 20% are In. The average In at. % for the bottom, middle and top QWs are 19.9 ± 4.2 at. %, 21.0 ± 4.1 at. % and 19.7 ± 4.4 at. %, respectively, in agreement with their nominal composition. However, the distribution of In within each QW varies, ranging from ~ 15 at. % near the interfaces to ~ 35 at. % at the centre of the QWs (Fig. 2 and Fig. S2). These variations are significant, as compositional asymmetry has been shown to induce shifts in the E_g [29, 41, 42]. For example, the middle QW exhibits an In concentration at its centre of ~ 30 at. %, equivalent to a composition of $\text{In}_{0.60}\text{Ga}_{0.40}\text{As}$, which would result in a E_g of $\sim 0.68\text{eV}$. This would represent a decrease in the E_g of $\sim 0.2\text{eV}$ compared to the expected E_g for $\text{In}_{0.40}\text{Ga}_{0.60}\text{As}$ of 0.894eV [43].

It is worth noting that the chemical composition appears less controllable in lasers grown on metamorphic buffers, likely due to the strain management required on what are overall non-planar surfaces. The surface displays a so-called crosshatched pattern, which may enhance In diffusion during growth [37]. While strain engineering is an alternative, and sometimes complementary, approach to varying the E_g variations in the In concentration are expected to further impact strain levels. Thus, the strain levels across all QWs are next investigated and correlated to the measured In concentration.

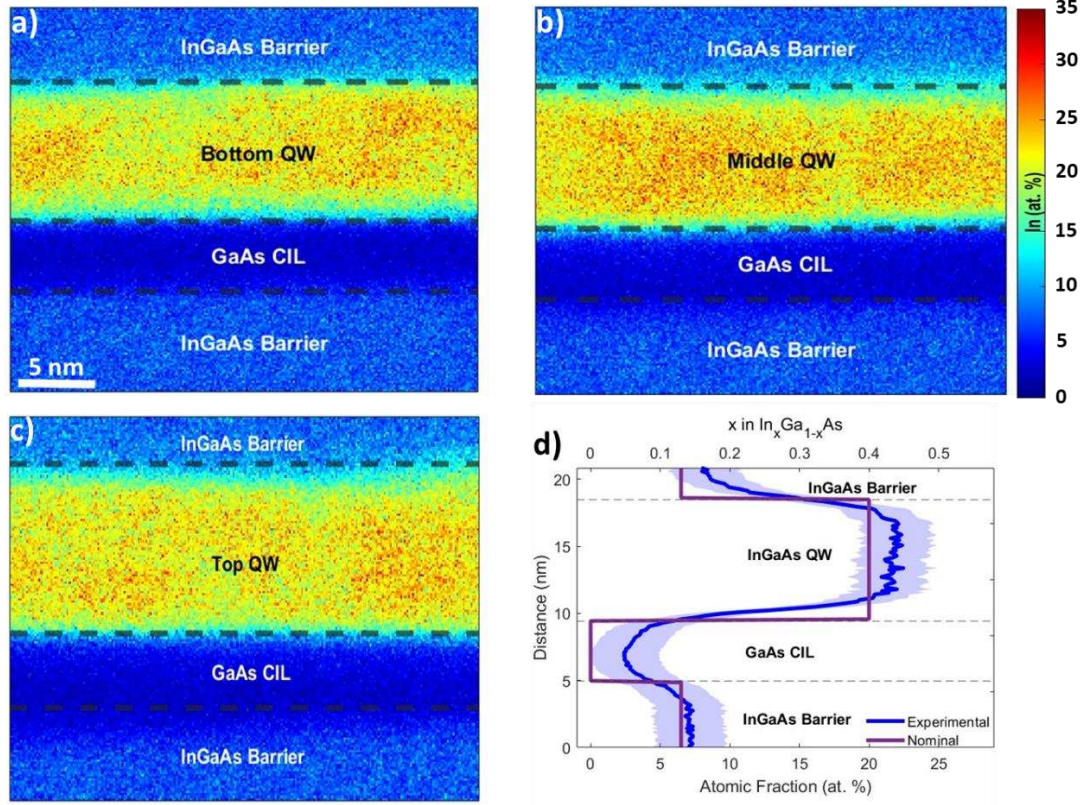


Figure 2. In at. % colour map for the bottom (a), middle (b) and top (c) QWs region, and representative In at. % profile for the top QW (d). The blue solid line denotes the experimentally measured In at. % with its uncertainty (shaded area). The secondary x axis indicates x in $\text{In}_x\text{Ga}_{1-x}\text{As}$.

Strain Analysis

The effect of strain on the E_g in III-V semiconductors has been both studied theoretically [20, 44, 45] and experimentally [46, 47]. Strain modifies energy levels of the orbitals, which depending on the strain and system, will change the E_g . Kuo *et al.* showed that biaxial tensile strain in $\text{In}_x\text{Ga}_{1-x}\text{As}$ epilayers on GaAs (and $\text{In}_x\text{Ga}_{1-x}\text{P}$ on InP) leads to a reduction in the E_g , while the opposite effect was observed for compressive strain [16]. Similarly, Gal *et al.* experimentally demonstrated that for $\text{In}_{0.17}\text{Ga}_{0.83}\text{As}$ QWs the magnitude and sign of strain can be altered as a function of thickness thereby inducing changes in the E_g [21]. Furthermore, it QWs is has been shown that for certain combinations of strain and QW thickness the quantum confinement can further affect the strain induced band modifications [18].

The strain for a film grown on a substrate (ε) is typically expressed as:

$$\varepsilon = \frac{a_l - a_{ref}}{a_l} \times 100\% \quad (\text{Eq 1})$$

Where a_l is the lattice constant of the layer of interest and a_{ref} is the lattice constant of the reference layer. In this work, the $\text{In}_{0.13}\text{Ga}_{0.87}\text{As}$ barrier is used as the reference region for all strain measurements here presented, which based on Vegard's law has a lattice constant of 5.7059\AA . It should be noted that the experimental In at. % for the $\text{In}_{0.13}\text{Ga}_{0.87}\text{As}$ reference region was found within the nominal concentration (Fig. 2d and S2) and thus no significant change in the lattice parameter is expected.

In previous work [48], we demonstrated that for these type of metamorphic lasers the general trend is that the strain varies significantly along the growth direction, having either compressive or tensile strain, while the strain parallel to the interface remains largely homogenous. The sample investigated in this work exhibits the same trend. Figure 3 shows the strain along the growth direction [200] (ϵ_{yy}) for all QWs, the full analysis is detailed in the SI. Negative strain values indicate tensile strain relative to the reference region ($\text{In}_{0.13}\text{Ga}_{0.87}\text{As}$ barrier), whereas positive values indicate compressive strain.

Considering the lattice constants of the nominal concentrations for the $\text{In}_{0.40}\text{Ga}_{0.60}\text{As}$ QWs, and $\text{In}_{0.13}\text{Ga}_{0.87}\text{As}$ barrier, are 5.8152\AA and 5.7059\AA , respectively, it is expected (as per Eq. 1) that the strain in the QWs will be compressive. On the other hand, the GaAs CIL possesses a smaller lattice constant (5.6532\AA) than the $\text{In}_{0.13}\text{Ga}_{0.87}\text{As}$ barrier (5.7059\AA), resulting in a negative strain value indicating tensile strain. The measured strain analysis confirms that in the growth direction the GaAs CIL layer is under tensile strain, and the QWs are under compressive strain (Fig. 3). The average ϵ_{yy} strain values indicate that the strain is highest for the top QW and lowest for the middle QW, with the top and bottom QWs exhibiting similar values: $2.71\pm 1.62\%$ for the top QW, $0.95\pm 4.93\%$ for the middle QW and $2.33\pm 1.59\%$ for the bottom QW. The uncertainties quoted are the standard deviation, as outlined in the SI. The strain value for the middle QW is unexpected, it exhibits areas of tensile strain, leading to a reduction in overall strain and a higher uncertainty. The reason for this is unclear given there is not significant difference in the In concentration compared to the other QWs. A possible source of error could arise from the strain difference between the nominal concentration $\text{In}_{0.40}\text{Ga}_{0.60}\text{As}$ and the reference area ($\text{In}_{0.13}\text{Ga}_{0.87}\text{As}$), which is 1.88% . However, the strain analysis for all three QWs falls within 1.88% , considering uncertainties. Additionally, extensive analysis was trailed under different conditions for this region which resulted in similar trends with different considerations and possible artefacts on the processing of the STEM images for geometric phase analysis (GPA) examined to ensure the accuracy of the strain maps (see SI, Figs. S4-S9).

The strain profiles for all QWs reach a maximum at the centres, as high as $\sim 4\%$ for the top and bottom QWs, which correlates with the higher In concentration at these points (Fig. 2.) Further agreement with the In concentration profiles is observed near the top and bottom interfaces (Fig. 3 and Fig. S10), where significant variations in the strain profile are evident for all QWs. Despite this qualitatively agreement with the In concentration, the measured strain values in the QWs greatly differ from the expected values based on the measured In concentration. For example, the strain at the centre of the

top QW (4nm from the GaAs interface) is $3.81 \pm 1.07\%$ with respect to $\text{In}_{0.13}\text{Ga}_{0.87}\text{As}$ barrier. According to Vegard's law, this strain would correspond to an In concentration of $\text{In}_{0.68}\text{Ga}_{0.32}\text{As}$, equivalent to 34 at. % In. However, this estimated concentration greatly exceeds the measured In concentration at this point (22.11 ± 2.86 at. %). A similar deviation is observed for the middle QW, where the strain measured at the centre ($\epsilon_{yy} = 0.19 \pm 7.97\%$) would indicate an unrealistically low In concentration (7.95 ± 7.95 at. %). While there is a clear correlation between chemical composition and strain, the discrepancy in the values highlights the complexity of quantitatively correlating strain and composition measurements. This suggests that other mechanisms may be influencing the results. Having identified variations for the In concentration and strain, the next section delves into measuring the E_g across all QWs.

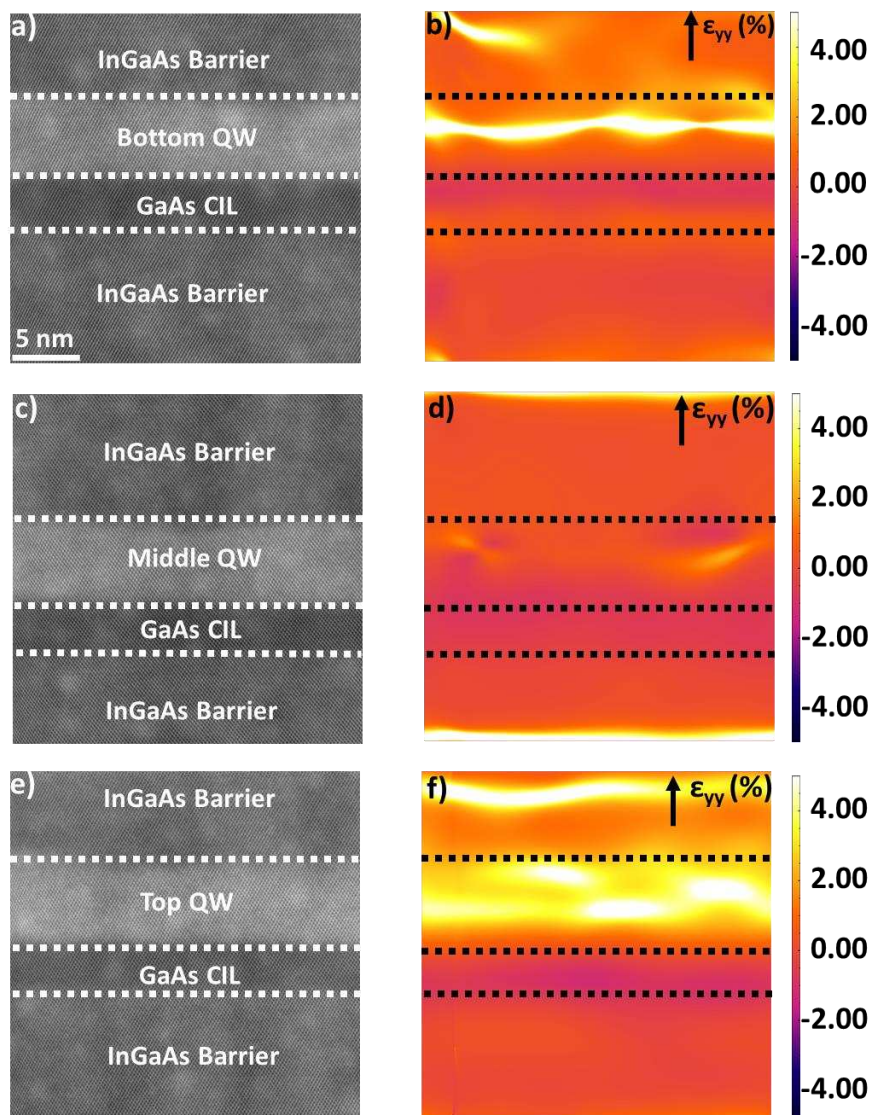


Figure 3. Strain analysis. HAADF-STEM viewed down $[1\ 1\ 0]$ zone axis image (a,c,e) and ϵ_{yy} strain map (b,d,f) for the bottom (a,b), middle (c,d) and top (e,f) QWs.

Bandgap measurements across multiple QWs

The optical E_g can be phenomenologically calculated as described by Nahroy *et al.* [43], which states that at 300K, the E_g of $\text{In}_x\text{Ga}_{1-x}\text{As}$ can be expressed in terms of the In mole fraction (x), as defined in Equation 2:

$$E_g(x) = 1.425\text{eV} - x \cdot 1.501\text{eV} + x^2 \cdot 0.436\text{eV} \quad (\text{Eq. 2})$$

For the nominal QWs composition of $\text{In}_{0.40}\text{Ga}_{0.60}\text{As}$, the expected E_g is 0.894eV. While this equation does not consider the QW thickness which is known to affect the E_g in $\text{In}_x\text{Ga}_{1-x}\text{As}$ QWs [49], it does provide a good approximation given that all QWs are nominally identical. Additionally band bending [50] is not expected to significantly impact the QWs due to the relatively large separation between them in the laser structure, allowing each QW to be considered independently.

Low-loss EELS was used to measure the E_g across all QWs. The spectra was corrected for Cerenkov radiation as described in the methods and SI, following the procedure published in [27]. Cerenkov radiation is emitted when electrons travel faster than light through a medium, causing a reduction in the measured E_g [51, 52]. The corrected E_g values show the same trend as the uncorrected data, but with higher E_g values (Fig. S12). Figure 4b summarises the spatially resolved E_g measured across all QWs, from the bottom (position 1) to the top interface (position 6), as indicated by the yellow rectangles in Fig. 4a and marked by the arrow. Full E_g profiles for the adjacent layers are presented in Fig. S13. The average E_g values for the QWs are $0.900 \pm 0.017\text{eV}$ for the top QW, $0.923 \pm 0.015\text{eV}$ for the middle QW and $0.883 \pm 0.021\text{eV}$ for the bottom QW (Fig. 5a). This indicates a variation between individual QWs, with the bottom QW having the lowest E_g , followed by the top QW and the middle QW having the highest E_g .

These values are within the range of the sample's bulk emission measured by photoluminescence (PL) [37] (Fig. S14) which has the main emission peak at $\sim 1360\text{nm}$ ($E_g = 0.914\text{eV}$) with a full width half maximum extending from 1320nm to 1410nm ($E_g = 0.941\text{eV} - 0.881\text{eV}$). Interestingly, subtle spatial variations within the individual QWs can be observed, particularly for the bottom QW which exhibits an apparent asymmetry near the interfaces, with the E_g values increasing towards the $\text{In}_{0.13}\text{Ga}_{0.87}\text{As}$ barrier and decreasing towards the bottom GaAs CIL. The subtle fluctuations in E_g with and between individual QWs is lost when EELS is acquired over all 3 QWs due to the lower spatial resolution (Fig. S16), further highlighting the importance of spatially resolved measurements.

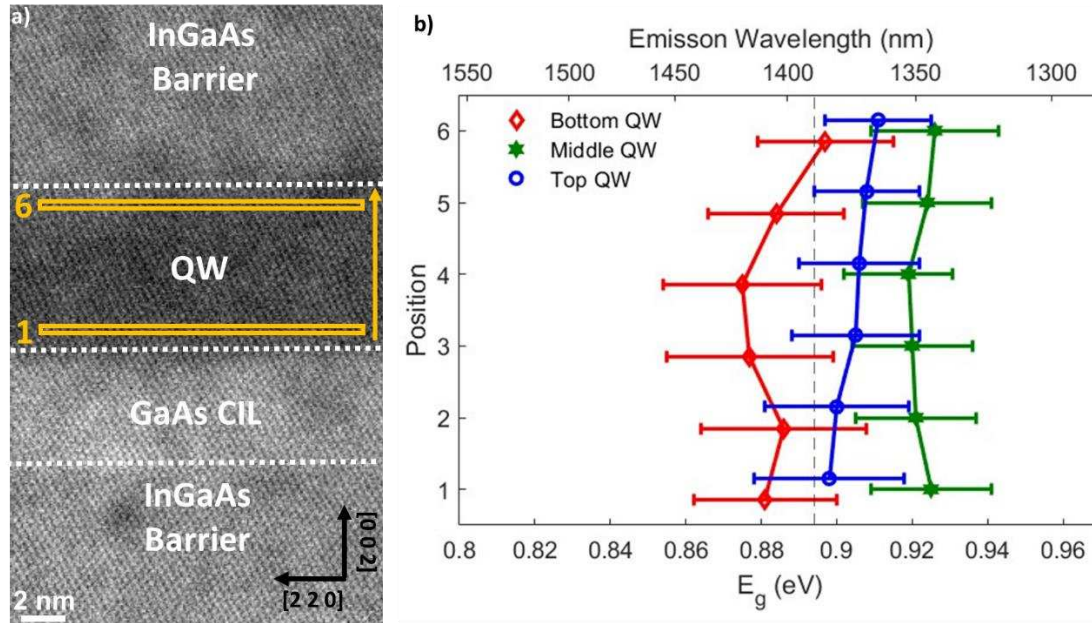


Figure 4. E_g analysis. Representative HAADF-STEM image of the middle QWs (a), and the corresponding measured E_g (b) corrected for Cerenkov: bottom (red diamond), middle (green hexagon) and top QW (blue circle). The E_g was measured horizontally as indicated by the yellow markings in a). The secondary axis shows the corresponding emission wavelength. The dashed grey line represents the calculated E_g for $In_{0.40}Ga_{0.60}As$ from Nahroy et al. [43].

Correlating the strain trends to the measured E_g , both the average ϵ_{yy} strain and E_g do not significantly differ between the bottom and top QWs, while the middle QW exhibits the lowest average strain values and the highest E_g (0.923 ± 0.015 eV). The strain is at its lowest near the GaAs interface, consistent with the In content. Thus, a similar trend would be expected for the E_g . However, surprisingly, only the bottom QW shows slightly different values for the calculated E_g near the interfaces, albeit asymmetric.

Thickness variations in the lamella were considered as a potential source of the differences in the measured E_g . Relative thickness (t/λ) varies from ~ 0.42 to 0.52 t/λ across the QWs, with the lamella thickness slightly increasing at the centre of the of the QW (Fig. S15). However, this is not reflected in the measured E_g , indicating that the thickness variations between individual QWs are not large enough to influence the E_g measurements.

To better understand these variations, we consider the composition effect on the E_g . Figure 5a shows the measured average E_g and In concentration for each QW. All values are near the E_g calculated using Eq. 2 (dashed purple line in Fig. 5a) and within the PL measurements, demonstrating that the E_g values calculated from low-loss EELS are reasonable. However, subtle variations in the E_g are evident values across the QWs, particularly within the bottom QW (Fig. 5b) where an asymmetry is more

apparent, with only the central values falling within the expected range for the measured In concentration, after accounting for uncertainties.

Density Functional Theory (DFT) simulations were conducted to further understand the effects of strain and composition on the E_g , and correlate these to the observed trends for the measured E_g . Figure 5c-d present the simulated low-loss EELS for various $\text{In}_x\text{Ga}_{1-x}\text{As}$ alloys under different strain. These simulations consider the strain to be uniaxial (as shown in the inset in Fig. 5d) and do not account for surface effects or Cerenkov radiation. Moreover, DFT underestimates the onset energy and in turn E_g due to derivative discontinuity [53, 54]. Despite these limitations, this approach is known to have good reproducibility, making it ideal for identifying trends related to changes in strain and chemical composition [55, 56].

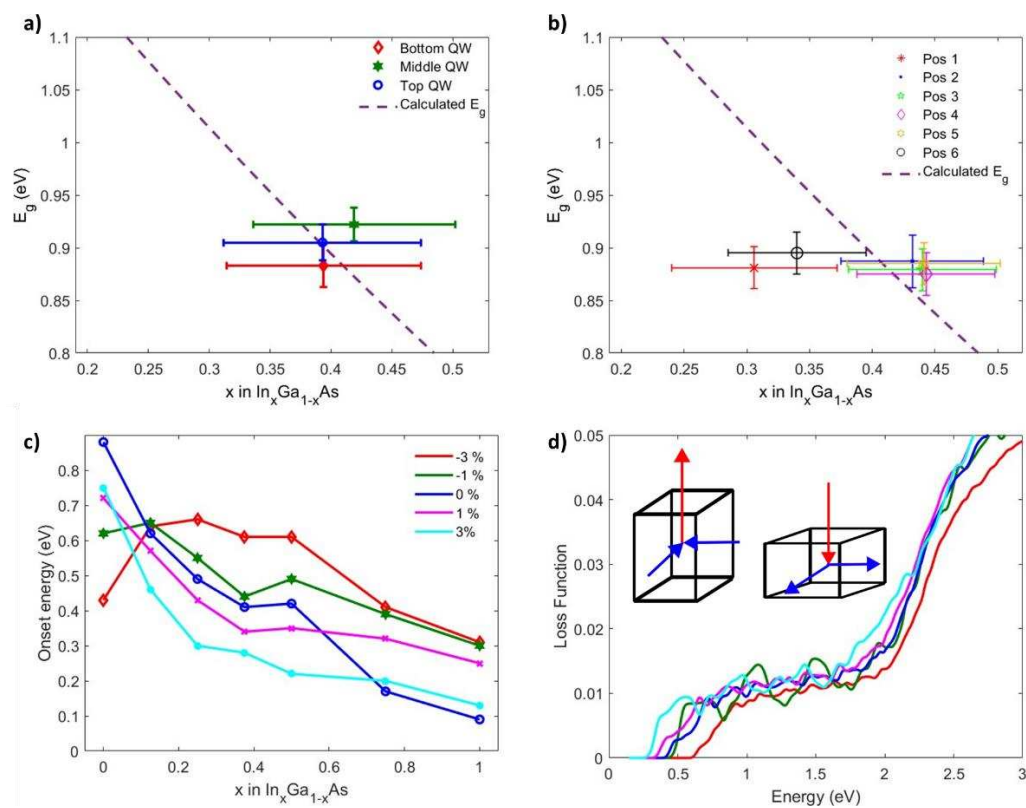


Figure 5. Comparison of the calculated E_g value and average measured E_g values for all QWs (a) and E_g values at each position (1-6) in the bottom QW (b) as function of In mole fraction (x). The calculated E_g as a function of x (dotted purple line) based on Eq. 2, from Nahroy et al. [45]. Simulated EELS energy onset as a function of x in $\text{In}_x\text{Ga}_{1-x}\text{As}$ (c) and for $\text{In}_{0.375}\text{Ga}_{0.625}\text{As}$ as a function of strain (d). Insert in 5d is a schematic of the uniaxial strain applied in the simulation.

Figure 5c shows the onset energy as a function of x in $\text{In}_x\text{Ga}_{1-x}\text{As}$. In general, the simulations indicate that irrespective of the strain regimen energy onset decreases as the In concentration increases, with

the most drastic changes observed for the highest strain magnitudes. For compositions between $x = 0.1 - 0.6$ the compressive strain exhibits the lowest energy onset values compared to tensile strain. Figure 5d plots the change in the energy onset and the corresponding loss function for the $\text{In}_{0.375}\text{Ga}_{0.625}\text{As}$ composition, close to the QWs nominal composition ($\text{In}_{0.40}\text{Ga}_{0.60}\text{As}$), as a function of strain. Additional plots for other compositions are shown in Fig. S19. For this composition, the energy onset is lower for high compressive strain values and shifts to higher energies for larger tensile strain values. Further highlighting that high strain magnitudes are needed to significantly affect the E_g , in agreement with previous reports [45], and indicating that the In content plays a more predominant role in the resulting E_g for a wide range of compositions and relatively low strain values. This provides a more direct correlation for the E_g variations observed between the individual QW's and within them.

While these trends provide significant insights, they suggest there may be additional factors influencing the measured E_g . This opens up exciting avenues for further investigations into effects such as interface effects, where imperfections from the growth can lead to rough or asymmetric boundaries between layers that may induce offsets which can alter the E_g [57, 58]. Previous work in other QW systems have demonstrated that interface fluctuations can have a pronounced impact for thinner QWs [6].

Conclusions

This study presents a comprehensive analysis of spatially resolved E_g across multiple $\text{In}_x\text{Ga}_{1-x}\text{As}$ QWs in a metamorphic laser structure, employing STEM and low-loss EELS. It explores the influence of In concentration and strain on the E_g , to two main factors widely accepted to influence it.

Our findings reveal significant variations in In concentration within the QWs, particularly near the interfaces. GPA strain mapping confirmed that the QWs are under compressive strain, with the strain values varying along the growth direction (ϵ_{yy}). Qualitative agreement was found between the fluctuations in the In concentration and strain. The average E_g values were found to be in the range of 0.89eV-0.92eV, close to the predicted 0.90eV for the QWs' nominal In concentration and within the range of the bulk emission measured by PL. Importantly, clear variations between individual QWs and subtle changes within the QWs (particularly for the bottom QW) were observed, revealing details that are lost in the bulk measurements. DFT simulations support the overall observed trends, indicating that the In content plays a predominant role in influencing the E_g . However, the fluctuations in the E_g values across individual QWs could not be directly correlated to strain or composition alone.

Our results underscore the critical role of nanoscale composition and strain management in determining the electronic and optical properties of metamorphic lasers. The discrepancy between measured and predicted values suggests the influence of other factors such as interface and surface

effects. Moreover, it highlights the need for further simulations where the size of the QW and local ordering is considered.

Overall, these results offer a valuable insight that can inform the design of the next-generation metamorphic lasers, highlighting the effect of localised chemical inhomogeneity and strain on the final device emission.

Methodology

Sample. The $\text{In}_{0.40}\text{Ga}_{0.60}\text{As}$ QW/GaAs metamorphic laser sample was grown via metal organic vapour phase epitaxy (MOVPE), detailed growth conditions and purity levels are reported elsewhere [37, 60]. Lamella were prepared using a TESCAN Lyra 3 dual beam Focussed Ion Beam/Scanning Electron Microscope (FIB/SEM) via conventional *in-situ* lift out procedure [61]. Lamella were further thinned using a Gatan Precision Ion Polishing System (PIPS) II system, followed by a final cleaning with a Fischione Model 1040 NanoMill, and baked at 125°C overnight prior to EELS acquisition.

Electron Microscopy Techniques. A Nion UltraSTEM 100MC 'HERMES', fitted with an energy resolution monochromator and cold field emission gun, was used to perform EELS and STEM imaging [62]. The operating voltage for EELS and STEM were 60kV. The electron optics were adjusted to a convergence angle of 30mrad and a probe size of $\sim 1.4\text{\AA}$. EELS spectrum images were recorded with a NION IRIS high energy resolution spectrometer equipped with a Dectris ELA hybrid pixel direct counting electron detector. The energy resolution of the experiments was $\sim 30\text{meV}$ determined by the monochromator selection slit. The collection angle of EELS was 44mrad and spectra were acquired at 5meV/channel. All raw EELS spectra were aligned and denoised using principal component analysis (PCA) before analysis [63], as detailed in the SI. Additional imaging was performed on the Nion UltraSTEM 100 electron microscope operated at 100kV. The electron optics were adjusted to a convergence angle of 30mrad and a probe size of $\sim 0.9\text{\AA}$. HAADF images were acquired as a rotational frame series (90° between frames), to eliminate stage drift and scanning distortions. The dataset were averaged by rigid and non rigid registration [64].

Energy dispersive X-ray spectroscopy (EDX) was acquired with a Thermofischer Talos F200-X at 200kV equipped with four in column Super X detector at an angle of 0.9sr, with a dwell time of 30ms and a pixel size of 0.131nm. For elemental quantification, $K\alpha$ peaks were used to quantify Ga and As while In was quantified with the $L\alpha$ peak. Background corrections were done using Brown-Powell Ionization cross section model [65]. In atomic fraction (at. %) maps were generated from extracting the In at. % at each pixel in the recorded EDX dataset and applying a colour map in MATLAB.

Strain mapping was carried out using GPA [66] in Strain ++ [67] on HAADF-STEM images. For GPA analysis, the reference region is $\text{In}_{0.13}\text{Ga}_{0.87}\text{As}$, using the \mathbf{g} vectors $\mathbf{g}=\mathbf{2\bar{2}0}$ and $\mathbf{g}=\mathbf{002}$, with a mask size (3σ) of ~ 12.33 . All images presented in the main manuscript were cropped from 1024×1024 pixels to 750×750 pixels and not rotated with further details provided in the SI. Theoretical strain was calculated using the formula for strain in a layer outlined in Dunstan *et al.* [68], with lattice parameters derived by Vegard's law [15].

In order to measure the experimental E_g , we begin by preparing our data for optimal fitting. The zero-loss peak is removed from the three QWs by fitting a general power law model [69] and eliminate possible contributions from Cerenkov radiation. Further details on this process are provided in SI. Finally, once the spectrum is corrected, we divide the QWs into 6 horizontally equal-sized regions and obtain a global spectrum from each of them by summing the spectra of all the pixels in these regions. After preparing the spectrum and obtaining the 6 global spectra, we perform an automated fitting of the direct E_g

$$I \sim A(E - E_g)^{0.5} \quad (\text{Eq. 3})$$

Where I is intensity of the signal, A is a constant and E is Energy [41].

Simulations. DFT simulations were performed using the CASTEP code [70], a plane-wave and pseudopotential based implementation of DFT. The plane wave basis set was converged to 1500eV, with a Monkhorst Pack grid of $10 \times 10 \times 10$ points used throughout. This grid was optimised on the cell with the smallest real-space lattice parameters ensuring a minimum quality of calculation throughout. Structures were relaxed to better than an energy convergence of 2×10^{-5} eV per ion and a force convergence of 5×10^{-2} eV \AA^{-1} , with a stress convergence of better than 1MPa. The recently developed meta-Generalized Gradient Approximation (GGA) functional RSCAN [71] was used to perform the simulations, ensuring a state-of-the-art treatment of the electron correlations within the system. This functional will, as a semi-local functional, show the derivative discontinuity problem that leads to the underestimation of the E_g . Finally, post-processing of the loss function was performed with the OPTADOS package [72, 73] and an adaptive smearing [74] of 0.4eV.

Declarations

Acknowledgments

N. Stephen and M. Arredondo acknowledge the support of the Engineering and Physical Sciences Research Council (Grant number EP/S023321/1).

E. Pelucchi acknowledges the support of Science Foundation Ireland under Grant Numbers 15/IA/2864, 22/FFP-A/10930 and 12/RC/2276_P2.

D. Kepaptsoglou acknowledges the support of SuperSTEM, the National Research Facility for Advanced Electron Microscopy funded by the Engineering and Physical Sciences Research Council (Grant number EP/W021080/1).

We are grateful for computational support from the UK national high performance computing service, ARCHER2, for which access was obtained via the UKCP consortium and funded by EPSRC grant ref EP/X035891/1.

ICN2 acknowledges funding from Generalitat de Catalunya 2021SGR00457. This study is part of the advanced materials programme and was supported by MCIN with funding from the European Union NextGenerationEU (PRTR-C17.I1) and Generalitat de Catalunya. We acknowledge support from CSIC Interdisciplinary Thematic Platform (PTI +) on Quantum Technologies.

Author Contributions

N.S and M.A conceived and planned most the experiments. I.P-H, R.L, M.B and J.A provided the $\text{In}_x\text{Ga}_{1-x}\text{As}$ simulation and EELS correction work. N.S and D.K carried out the EELS experiments, with D.K providing support for the analysis. A.G, E.M and E.P provided the sample and contributed to the interpretation of the results alongside N.S and M.A. N.S took the lead in writing the manuscript. All authors provided critical feedback and helped shape the research, analysis, and manuscript.

Conflict of Interest

The authors declare no competing personal or financial conflicts of interest.

Data and code availability

Not applicable.

Supplementary information

Supplementary information document attached provides further details of calculations and procedures used for evaluating the E_g and strain analysis. The document also provides all figures, full table of results and additional analysis that were not included as part of the main text.

Ethical approval

Not applicable.

References

1. Tångring I, Wang SM, Sadeghi M, et al (2007) Metamorphic growth of 1.25–1.29 μm InGaAs quantum well lasers on GaAs by molecular beam epitaxy. *J Cryst Growth* 301–302:971–974
2. Huffaker DL, Deppe DG (1998) Electroluminescence efficiency of 1.3 μm wavelength InGaAs/GaAs quantum dots. *Appl Phys Lett* 73:520–522. <https://doi.org/10.1063/1.121920>
3. Arai M, Kobayashi W, Kohtoku M (2013) 1.3- μm Range Metamorphic InGaAs Laser With High Characteristic Temperature for Low Power Consumption Operation. *IEEE J Sel Top Quantum Electron* 19:1502207–1502207. <https://doi.org/10.1109/jstqe.2013.2247978>
4. Wu D, Wang H, Wu B, et al (2008) Low threshold current density 1.3 μm metamorphic InGaAs/GaAs quantum well laser diodes. *Electron Lett* 44:474–475. <https://doi.org/10.1049/el:20080106>
5. Uchida T, Kurakake H, Soda H, Yamazaki S (1994) 1.3 μm InGaAs/GaAs strained quantum well lasers with InGaP cladding layer. *Electron Lett* 30:563–565. <https://doi.org/10.1049/el:19940378>
6. Camps I, Sanchez M, Gonzalez JC (2002) Efficiencies in multiquantum well lasers. *Semicond Sci Technol* 17:1013. <https://doi.org/10.1088/0268-1242/17/9/320>
7. Takemasa K, Munakata T, Kobayashi M, et al (1998) 1.3- μm AlGaInAs-AlGaInAs strained multiple-quantum-well lasers with a p-AlInAs electron stopper layer. *IEEE Photonics Technol Lett* 10:495–497. <https://doi.org/10.1109/68.662572>
8. Delfyett PJ (2003) Lasers, Semiconductor. In: Meyers RA (ed) *Encyclopedia of Physical Science and Technology* (Third Edition). Academic Press, New York, pp 443–475
9. Bugge F, Zeimer U, Wenzel H, et al (2006) Laser diodes with highly strained InGaAs MQWs and very narrow vertical far fields. *Phys Status Solidi C* 3:423–426. <https://doi.org/10.1002/pssc.200564120>
10. Alahyarizadeh Gh, Amirhoseiny M, Hassan Z (2015) Effect of QW thickness and numbers on performance characteristics of deep violet InGaN MQW lasers. *Int J Mod Phys B* 29:1550081. <https://doi.org/10.1142/S0217979215500812>
11. Saxena D, Jiang N, Yuan X, et al (2016) Design and Room-Temperature Operation of GaAs/AlGaAs Multiple Quantum Well Nanowire Lasers. *Nano Lett* 16:5080–5086. <https://doi.org/10.1021/acs.nanolett.6b01973>
12. Chen PA, Chang CY, Juang C (1993) Carrier-induced energy shift in GaAs/AlGaAs multiple quantum well laser diodes. *IEEE J Quantum Electron* 29:2607–2618. <https://doi.org/10.1109/3.250382>
13. Sizov DS, Bhat R, Zakharian A, et al (2010) Impact of Carrier Transport on Aquamarine–Green Laser Performance. *Appl Phys Express* 3:122101. <https://doi.org/10.1143/APEX.3.122101>

14. Zhukov AE, Kovsh AR, Mikhrin SS, et al (2003) Metamorphic Lasers for 1.3- μm Spectral Range Grown on GaAs Substrates by MBE. *Phys Semicond Devices* 37:1119–1122. <https://doi.org/10.1134/1.1610131>
15. Vurgaftman I, Meyer JR, Ram-Mohan LR (2001) Band parameters for III–V compound semiconductors and their alloys. *J Appl Phys* 89:5815–5875. <https://doi.org/10.1063/1.1368156>
16. Kuo CP, Vong SK, Cohen RM, Stringfellow GB (1985) Effect of mismatch strain on band gap in III-V semiconductors. *J Appl Phys* 57:5428–5432. <https://doi.org/10.1063/1.334817>
17. Shiri D, Kong Y, Buin A, Anantram MP (2008) Strain induced change of bandgap and effective mass in silicon nanowires. *Appl Phys Lett* 93:073114. <https://doi.org/10.1063/1.2973208>
18. Thijs PJA, Tiemeijer LF, Binsma JJM, Van Dongen T (1995) Strained-layer InGaAs(P) quantum well semiconductor lasers and semiconductor laser amplifiers. *Philips J Res* 49:187–224. [https://doi.org/10.1016/0165-5817\(95\)98697-V](https://doi.org/10.1016/0165-5817(95)98697-V)
19. Petó J, Dobrik G, Kukucska G, et al (2019) Moderate strain induced indirect bandgap and conduction electrons in MoS₂ single layers. *Npj 2D Mater Appl* 3:39. <https://doi.org/10.1038/s41699-019-0123-5>
20. Sweeney SJ, Eales TD, Adams AR (2019) The impact of strained layers on current and emerging semiconductor laser systems. *J Appl Phys* 125:082538. <https://doi.org/10.1063/1.5063710>
21. Gal M, Orders PJ, Usher BF, et al (1988) Observation of compressive and tensile strains in InGaAs/GaAs by photoluminescence spectroscopy. *Appl Phys Lett* 53:113–115. <https://doi.org/10.1063/1.100385>
22. Sun Y, Thompson SE, Nishida T (2007) Physics of strain effects in semiconductors and metal-oxide-semiconductor field-effect transistors. *J Appl Phys* 101:104503. <https://doi.org/10.1063/1.2730561>
23. Makuła P, Pacia M, Macyk W (2018) How To Correctly Determine the Band Gap Energy of Modified Semiconductor Photocatalysts Based on UV–Vis Spectra. *J Phys Chem Lett* 9:6814–6817. <https://doi.org/10.1021/acs.jpcclett.8b02892>
24. Sushko PV, Chambers SA (2020) Extracting band edge profiles at semiconductor heterostructures from hard-x-ray core-level photoelectron spectra. *Sci Rep* 10:13028. <https://doi.org/10.1038/s41598-020-69658-9>
25. Reshchikov MA (2021) Measurement and analysis of photoluminescence in GaN. *J Appl Phys* 129:121101. <https://doi.org/10.1063/5.0041608>
26. Erni R, Browning ND (2007) Quantification of the size-dependent energy gap of individual CdSe quantum dots by valence electron energy-loss spectroscopy. *Ultramicroscopy* 107:267–273. <https://doi.org/10.1016/j.ultramic.2006.08.002>
27. Martí-Sánchez S, Botifoll M, Oksenberg E, et al (2022) Sub-nanometer mapping of strain-induced band structure variations in planar nanowire core-shell heterostructures. *Nat Commun* 13:4089. <https://doi.org/10.1038/s41467-022-31778-3>
28. Krivanek OL, Dellby N, Hachtel JA, et al (2019) Progress in ultrahigh energy resolution EELS. *Ultramicroscopy* 203:60–67. <https://doi.org/10.1016/j.ultramic.2018.12.006>

29. Zhan W, Venkatachalapathy V, Aarholt T, et al (2018) Band gap maps beyond the delocalization limit: correlation between optical band gaps and plasmon energies at the nanoscale. *Sci Rep* 8:848. <https://doi.org/10.1038/s41598-017-18949-9>
30. Zhan W, Granerød CS, Venkatachalapathy V, et al (2017) Nanoscale mapping of optical band gaps using monochromated electron energy loss spectroscopy. *Nanotechnology* 28:105703. <https://doi.org/10.1088/1361-6528/aa5962>
31. Keller D, Buecheler S, Reinhard P, et al (2014) Local Band Gap Measurements by VEELS of Thin Film Solar Cells. *Microsc Microanal* 20:1246–1253. <https://doi.org/10.1017/S1431927614000543>
32. Wei J, Ogawa T, Feng B, et al (2020) Direct Measurement of Electronic Band Structures at Oxide Grain Boundaries. *Nano Lett* 20:2530–2536. <https://doi.org/10.1021/acs.nanolett.9b05298>
33. Brokkelkamp A, ter Hoeve J, Postmes I, et al (2022) Spatially Resolved Band Gap and Dielectric Function in Two-Dimensional Materials from Electron Energy Loss Spectroscopy. *J Phys Chem A* 126:1255–1262. <https://doi.org/10.1021/acs.jpca.1c09566>
34. Pelaez-Fernandez M, Lin Y-C, Suenaga K, Arenal R (2021) Optoelectronic Properties of Atomically Thin $\text{Mo}_x\text{W}_{(1-x)}\text{S}_2$ Nanoflakes Probed by Spatially-Resolved Monochromated EELS. *Nanomaterials* 11:3218. <https://doi.org/10.3390/nano11123218>
35. Kadkhodazadeh S, Ashwin MJ, Jones TS, McComb DW (2008) Towards measuring bandgap inhomogeneities in InAs/GaAs quantum dots. *J Phys Conf Ser* 126:012049. <https://doi.org/10.1088/1742-6596/126/1/012049>
36. Beznasyuk DV, Martí-Sánchez S, Kang J-H, et al (2022) Doubling the mobility of InAs/InGaAs selective area grown nanowires. *Phys Rev Mater* 6:034602. <https://doi.org/10.1103/PhysRevMaterials.6.034602>
37. Mura EE, Gocalinska AM, O'Brien M, et al (2021) Importance of Overcoming MOVPE Surface Evolution Instabilities for >1.3 μm Metamorphic Lasers on GaAs. *Cryst Growth Des* 21:2068–2075. <https://doi.org/10.1021/acs.cgd.0c01498>
38. Mura E (2019) MOVPE metamorphic lasers and nanostructure engineering at telecom wavelengths. PhD Dissertation, University College Cork
39. Goetz KH, Bimberg D, Jürgensen H, et al (1983) Optical and crystallographic properties and impurity incorporation of $\text{Ga}_x\text{In}_{1-x}\text{As}$ ($0.44 < x < 0.49$) grown by liquid phase epitaxy, vapor phase epitaxy, and metal organic chemical vapor deposition. *J Appl Phys* 54:4543–4552. <https://doi.org/10.1063/1.332655>
40. Fleischmann T, Moran M, Hopkinson M, et al (2001) Strained layer (111)B GaAs/InGaAs single quantum well lasers and the dependence of their characteristics upon indium composition. *J Appl Phys* 89:4689–4696. <https://doi.org/10.1063/1.1359155>
41. Granerød CS, Zhan W, Prytz Ø (2018) Automated approaches for band gap mapping in STEM-EELS. *Ultramicroscopy* 184:39–45. <https://doi.org/10.1016/j.ultramic.2017.08.006>
42. Gadre CA, Yan X, Song Q, et al (2022) Nanoscale imaging of phonon dynamics by electron microscopy. *Nature* 606:292–297. <https://doi.org/10.1038/s41586-022-04736-8>

43. Nahory RE, Pollack MA, Johnston WD, Barns RL (1978) Band gap versus composition and demonstration of Vegard's law for $\text{In}_{1-x}\text{Ga}_x\text{As}_y\text{P}_{1-y}$ lattice matched to InP. *Appl Phys Lett* 33:659–661. <https://doi.org/10.1063/1.90455>
44. Olsen GH, Nuese CJ, Smith RT (1978) The effect of elastic strain on energy band gap and lattice parameter in III-V compounds. *J Appl Phys* 49:5523–5529. <https://doi.org/10.1063/1.324472>
45. Mondal B, Tonner-Zech R (2023) Systematic strain-induced bandgap tuning in binary III–V semiconductors from density functional theory. *Phys Scr* 98:065924. <https://doi.org/10.1088/1402-4896/acd08b>
46. Aumer ME, LeBoeuf SF, Bedair SM, et al (2000) Effects of tensile and compressive strain on the luminescence properties of AlInGaN/InGaN quantum well structures. *Appl Phys Lett* 77:821–823. <https://doi.org/10.1063/1.1306648>
47. Chen JF, Wang PY, Wang JS, et al (2000) Strain relaxation in $\text{In}_{0.2}\text{Ga}_{0.8}\text{As}/\text{GaAs}$ quantum-well structures by x-ray diffraction and photoluminescence. *J Appl Phys* 87:1251–1254. <https://doi.org/10.1063/1.372004>
48. Stephen N, Kumar P, Gocalinska A, et al (2023) Dislocation and strain mapping in metamorphic parabolic-graded InGaAs buffers on GaAs. *J Mater Sci* 58:9547–9561. <https://doi.org/10.1007/s10853-023-08597-y>
49. Fonseka HA, Ameruddin AS, Caroff P, et al (2017) InP– $\text{In}_x\text{Ga}_{1-x}\text{As}$ core-multi-shell nanowire quantum wells with tunable emission in the 1.3–1.55 μm wavelength range. *Nanoscale* 9:13554–13562. <https://doi.org/10.1039/C7NR04598K>
50. Quang DN, Tung NH (2008) Band-bending effects on the electronic properties of square quantum wells. *Phys Rev B* 77:125335. <https://doi.org/10.1103/PhysRevB.77.125335>
51. Park J, Heo S, Chung J-G, et al (2009) Bandgap measurement of thin dielectric films using monochromated STEM-EELS. *Ultramicroscopy* 109:1183–1188. <https://doi.org/10.1016/j.ultramic.2009.04.005>
52. Horák M, Stöger-Pollach M (2015) The Čerenkov limit of Si, GaAs and GaP in electron energy loss spectrometry. *Ultramicroscopy* 157:73–78. <https://doi.org/10.1016/j.ultramic.2015.06.005>
53. Mori-Sánchez P, Cohen AJ (2014) The derivative discontinuity of the exchange–correlation functional. *Phys Chem Chem Phys* 16:14378–14387. <https://doi.org/10.1039/C4CP01170H>
54. Perdew JP, Parr RG, Levy M, Balduz JL (1982) Density-Functional Theory for Fractional Particle Number: Derivative Discontinuities of the Energy. *Phys Rev Lett* 49:1691–1694. <https://doi.org/10.1103/PhysRevLett.49.1691>
55. Lejaeghere K, Bihlmayer G, Björkman T, et al (2016) Reproducibility in density functional theory calculations of solids. *Science* 351:aad3000-1-aad3000-6. <https://doi.org/10.1126/science.aad3000>
56. Ji Y, Lin P, Ren X, He L (2022) Reproducibility of Hybrid Density Functional Calculations for Equation-of-State Properties and Band Gaps. *J Phys Chem A* 126:5924–5931. <https://doi.org/10.1021/acs.jpca.2c05170>

57. Oloumi M, Matthai CC (1991) Electronic structure of InGaAs and band offsets in InGaAs/GaAs superlattices. *J Phys Condens Matter* 3:9981. <https://doi.org/10.1088/0953-8984/3/50/004>
58. Tersoff J (1984) Theory of semiconductor heterojunctions: The role of quantum dipoles. *Phys Rev B* 30:4874–4877. <https://doi.org/10.1103/PhysRevB.30.4874>
59. Wang Y, Sheng X, Guo Q, et al (2017) Photoluminescence Study of the Interface Fluctuation Effect for InGaAs/InAlAs/InP Single Quantum Well with Different Thickness. *Nanoscale Res Lett* 12:229. <https://doi.org/10.1186/s11671-017-1998-8>
60. Dimastrodonato V, Mereni LO, Young RJ, Pelucchi E (2011) Relevance of the purity level in a Metal Organic Vapour Phase Epitaxy reactor environment for the growth of high quality pyramidal site-controlled Quantum Dots. *J Cryst Growth* 315:119–122. <https://doi.org/10.1016/j.jcrysgro.2010.09.011>
61. O'Reilly T, Holsgrove K, Gholinia A, et al (2022) Exploring domain continuity across BaTiO₃ grain boundaries: Theory meets experiment. *Acta Mater* 235:118096. <https://doi.org/10.1016/j.actamat.2022.118096>
62. Krivanek OL, Lovejoy TC, Murfitt MF, et al (2014) Towards sub-10 meV energy resolution STEM-EELS. *J Phys Conf Ser* 522:012023. <https://doi.org/10.1088/1742-6596/522/1/012023>
63. Bonnet N, Brun N, Colliex C (1999) Extracting information from sequences of spatially resolved EELS spectra using multivariate statistical analysis. *Ultramicroscopy* 77:97–112. [https://doi.org/10.1016/S0304-3991\(99\)00042-X](https://doi.org/10.1016/S0304-3991(99)00042-X)
64. Jones L, Yang H, Pennycook TJ, et al (2015) Smart Align—a new tool for robust non-rigid registration of scanning microscope data. *Adv Struct Chem Imaging* 1:8. <https://doi.org/10.1186/s40679-015-0008-4>
65. Powell CJ (1976) Evaluation of Formulas for Inner-shell Ionization Cross Sections. *NIST* 460:97–104
66. Hÿtch MJ, Snoeck E, Kilaas R (1998) Quantitative measurement of displacement and strain fields from HREM micrographs. *Ultramicroscopy* 74:131–146. [https://doi.org/10.1016/S0304-3991\(98\)00035-7](https://doi.org/10.1016/S0304-3991(98)00035-7)
67. Peters JJP Strain ++, <http://jjppeters.github.io/Strainpp/>
68. Dunstan DJ (1997) Strain and strain relaxation in semiconductors. *J Mater Sci Mater Electron* 8:337–375. <https://doi.org/10.1023/A:1018547625106>
69. Fung KLY, Fay MW, Collins SM, et al (2020) Accurate EELS background subtraction – an adaptable method in MATLAB. *Ultramicroscopy* 217:113052. <https://doi.org/10.1016/j.ultramic.2020.113052>
70. Clark SJ, Segall MD, Pickard CJ, et al (2005) First principles methods using CASTEP. *Z Für Krist - Cryst Mater* 220:567–570. <https://doi.org/10.1524/zkri.220.5.567.65075>
71. Bartók AP, Yates JR (2019) Regularized SCAN functional. *J Chem Phys* 150:161101. <https://doi.org/10.1063/1.5094646>

72. Nicholls RJ, Morris AJ, Pickard CJ, Yates JR (2012) OptaDOS - a new tool for EELS calculations. *J Phys Conf Ser* 371:012062. <https://doi.org/10.1088/1742-6596/371/1/012062>
73. Morris AJ, Nicholls RJ, Pickard CJ, Yates JR (2014) OptaDOS: A tool for obtaining density of states, core-level and optical spectra from electronic structure codes. *Comput Phys Commun* 185:1477–1485. <https://doi.org/10.1016/j.cpc.2014.02.013>
74. Yates JR, Wang X, Vanderbilt D, Souza I (2007) Spectral and Fermi surface properties from Wannier interpolation. *Phys Rev B* 75:195121. <https://doi.org/10.1103/PhysRevB.75.195121>

Supplementary Information

In Atomic Fraction Mapping

The full structure of the metamorphic laser consists of a GaAs (001) substrate misoriented 6° towards $[1\ 1\ 1]_A$ with a $1\ \mu\text{m}$ thick parabolic graded $\text{In}_x\text{Ga}_{1-x}\text{As}$ metamorphic buffer (MB) with an In concentration varying nominally from $0 < x < 0.18$, deposited on top. After the MB, an $\text{Al}_x\text{In}_y\text{Ga}_{1-x-y}\text{As}/\text{In}_{0.62}\text{Ga}_{0.38}\text{P}$ superlattice n-type cladding layer is added with a separate confinement heterostructure (SCH) consisting of $\text{Al}_x\text{In}_y\text{Ga}_{1-x-y}\text{As}/\text{In}_{0.62}\text{Ga}_{0.38}\text{P}$ acting as the barrier layer to the active region. The active region consists of a repeated stacking of GaAs Interface Controlling layer (CIL), $\text{In}_{0.40}\text{Ga}_{0.60}\text{As}$ QW and an $\text{In}_{0.13}\text{Ga}_{0.87}\text{As}$ barrier layer as outlined in the main manuscript. After the active region, a second SCH layer is grown followed p-type $\text{Al}_x\text{In}_y\text{Ga}_{1-x-y}\text{As}/\text{In}_{0.62}\text{Ga}_{0.38}\text{P}$ SL cladding. Finally, an $\text{In}_x\text{Ga}_{1-x}\text{As}$ contact layer is placed after the cladding, completing the full structure. Further details and characterisation of this structure can be found in Mura *et al.* [1].

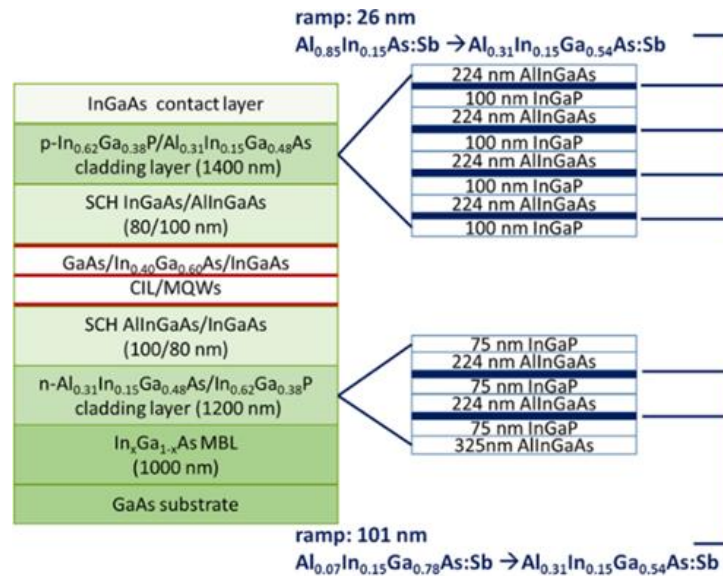


Figure S1. Schematic diagram of metamorphic laser investigated. From [1].

Given that the QW thickness can significantly impacts the bandgap (E_g), the thickness of each QW was measured and compared to their nominal thickness. Table S1 shows that the QWs have comparable thicknesses, slightly thicker than the nominal 7nm.

QW	Thickness (nm)
Bottom	8.54±0.17
Middle	8.64±0.10
Top	8.60±0.17

Table S1. Measured thickness of QWs.

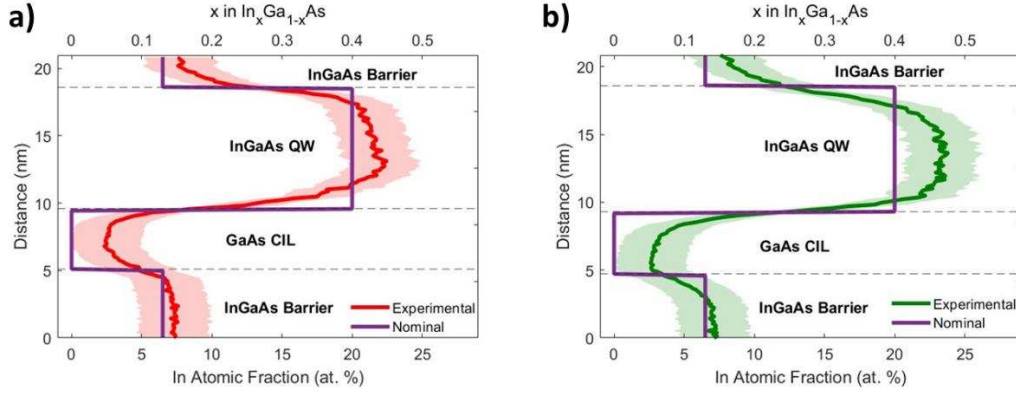


Figure S2. Atomic fraction profile for the bottom (a) and middle QW (b). The red/green solid line denote the experimentally measured In at. % and the shaded area correspond to the uncertainty in the bottom/middle QW respectively. The secondary x axis indicates to x in $\text{In}_x\text{Ga}_{1-x}\text{As}$.

Figure S2 shows the In atomic fraction profile for both the bottom and middle QWs. We see similar trends and In concentration values, as seen in the top QW (Fig. 2d in the main manuscript). The average In at. % is presented in Table S2, indicating that the average concentrations are similar to each other.

QW	In (at.%)
Bottom	19.9±4.2
Middle	21.0±4.1
Top	19.7±4.4

Table S2. Average In at.% across QWs.

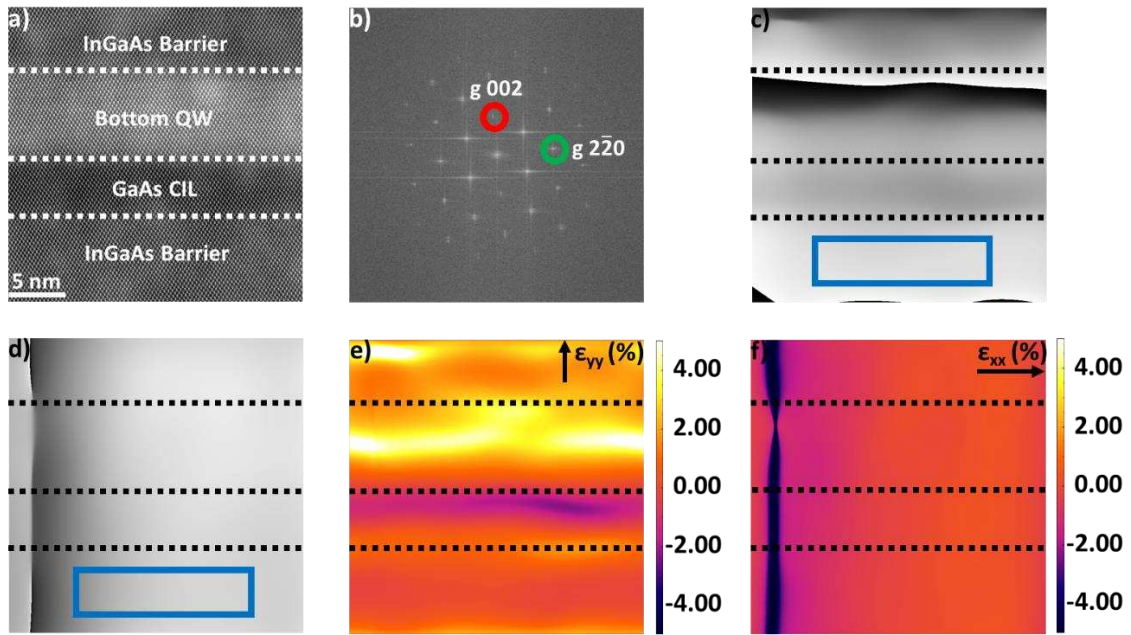
We also checked the concentration of the lower $\text{In}_{0.13}\text{Ga}_{0.87}\text{As}$ barrier, which will be used as a reference region in later Geometric Phase Analysis (GPA). Table S3 shows the In at. % in the lower $\text{In}_{0.13}\text{Ga}_{0.87}\text{As}$ barrier (the barrier layer below the GaAs CIL layer that is underneath the $\text{In}_{0.40}\text{Ga}_{0.60}\text{As}$ QW) near the bottom, middle and top QW are 6.8 ± 0.9 at.%, 6.6 ± 0.8 at.% and 6.6 ± 0.8 at.% respectively. These In at.% of nominal $\text{In}_{0.13}\text{Ga}_{0.87}\text{As}$ barrier is 6.5%, which the measured In at.% all three QW's are within. Therefore, in the theoretical strain calculations, we can use that the nominal $\text{In}_{0.13}\text{Ga}_{0.87}\text{As}$ barrier as reference region.

QW	In (at.%) of lower $\text{In}_{0.13}\text{Ga}_{0.87}\text{As}$ barrier
Bottom	6.8±0.9
Middle	6.6±0.8
Top	6.6±0.8

Table S3. Average In at.% in $\text{In}_{0.13}\text{Ga}_{0.87}\text{As}$ two layers below bottom, middle and top QW.

Strain Analysis

The first step for the strain analysis via GPA was to crop the HAADF-STEM from 1024x1024 pixels image to 850x850 pixels to reduce edge effects in the GPA analysis. Using a mask size (3σ) of 12.33 in Strain ++, the $\mathbf{g}=\mathbf{002}$ is selected in the Fast Fourier Transform (FFT) as shown in Fig. S3b. The phase map is then tuned in the lower $\text{In}_{0.13}\text{Ga}_{0.87}\text{As}$ barrier area until the phase map is homogenous as possible (Fig. S3c). This process is repeated using the $\mathbf{g}=\mathbf{2\bar{2}0}$ vector (Fig. S3d) with the final ϵ_{yy} (Fig.



S3e) and ϵ_{xx} (Fig. S3f) strain maps obtained.

Figure S3. Illustration process of GPA strain mapping using bottom QW. HAADF-STEM image viewed down $[1\ 1\ 0]$ zone axis of area of interest (a) and corresponding FFT image (b). Final phase after tuned with respect to the reference region using $\mathbf{g}=\mathbf{002}$ (c) and $\mathbf{g}=\mathbf{2\bar{2}0}$ (d). Convert final phase image to yield ϵ_{yy} (e) and ϵ_{xx} (f) strain map. Red and green circle in b represent mask location for $\mathbf{g}=\mathbf{002}$ and $\mathbf{g}=\mathbf{2\bar{2}0}$ respectively. Blue box in c and d represents reference region.

In GPA strain analysis, while qualitative observations are often discussed, precise quantitative information and the associated uncertainties are not extensively considered. For an average value of the strain measurements and similarly the In atomic fraction, two key expressions denote uncertainty within the values which are standard deviation (σ) and standard error (SE). σ quantifies the variation around the mean in a dataset and is mathematically expressed as

$$\sigma = \sqrt{\frac{\sum(x_i - \mu)^2}{N}} \quad (\text{Eq S1})$$

Where x_i represents a single data point, N is the total number of datapoints and μ is the mean. SE can be derived as

$$SE = \frac{\sigma}{\sqrt{N}} \quad (\text{Eq S2})$$

The differences between SE and σ will now be illustrated in an example using GPA strain measurements further detailed in the main manuscript. A line profile from the $\text{In}_{0.40}\text{Ga}_{0.60}\text{As}$ QW layer from the resultant ϵ_{yy} strain map (see Fig. S4) was taken over an area of 378×53 pixels with each pixel representing a ϵ_{yy} datapoint.

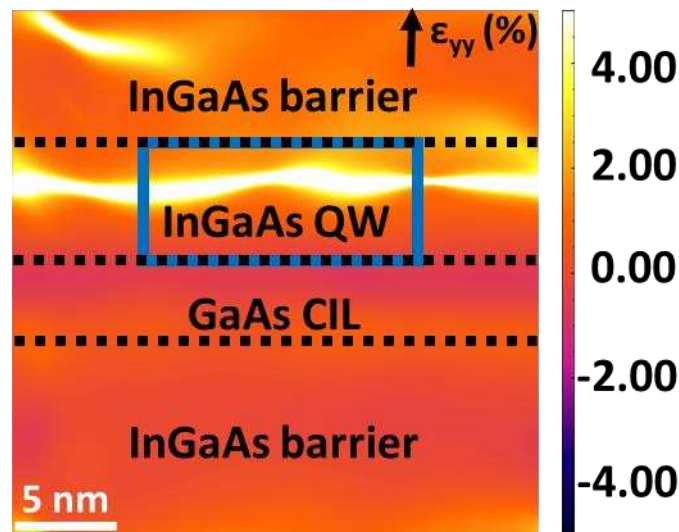


Figure S4. ϵ_{yy} strain map of $\text{In}_{0.40}\text{Ga}_{0.60}\text{As}$ bottom QW region (see manuscript).

Pixel size	ϵ_{yy}	σ	SE
378 x 53	2.33	1.59	0.01

Table S4. Average ϵ_{yy} , σ and SE in boxed region in Figure S4.

The recorded average strain ϵ_{yy} in the bottom QW (highlighted area in Fig. S4) is 2.33%, with an associated σ and SE of 1.59% and 0.01%, respectively, as shown in Table S4. The small SE value is attributed to the large number of pixels considered in the calculation. Since the area of interest exhibits fluctuations of $\sim 2\%$, quoting the standard deviation as the uncertainty for GPA in this investigation was considered to be a reasonable approach. Similar conclusions were seen with the middle and top QW with a similar argument applicable for quotation the In atomic fraction uncertainty in σ .

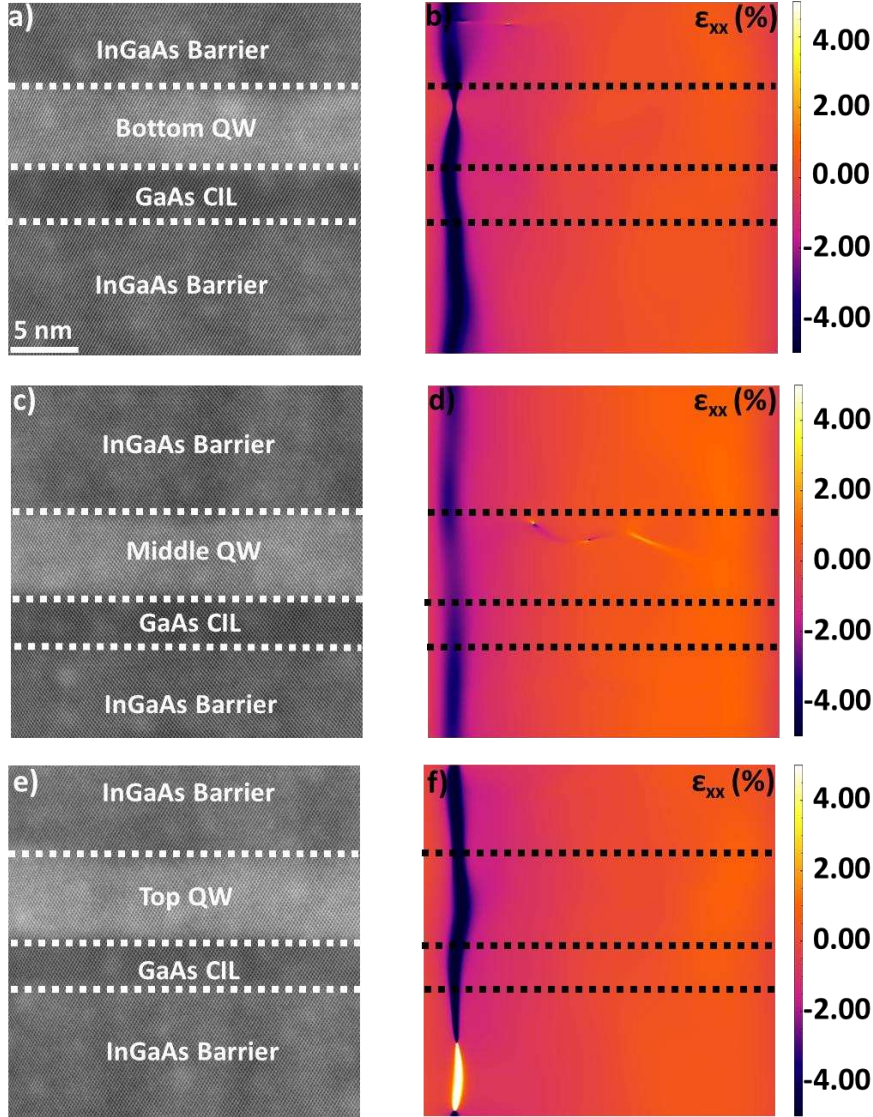


Figure S5. Strain analysis. HAADF-STEM viewed down $[1\ 1\ 0]$ zone axis images (a,c,e) and ϵ_{xx} (b,d,f) of bottom QW (a,b), middle QW (c,d) and top QW (e,f). All images cropped to pixel size 750 x 750.

To remove scanning artifacts in the initial HAADF-STEM image was attempted using a combination of cropping and rotation of the image. For cropping, a box was placed in the centre of the image as shown in Fig. S6b with parts of the images removed. The cropped image which does result in a change in the strain maps comparing both ϵ_{yy} (Fig. S6b with Fig. S6e) and ϵ_{xx} strain maps (Fig. S6c with Fig. S6f). The full ϵ_{yy} plot under the different cropping conditions for the bottom QW is presented in Fig. S7. After trialling the crop with all three $\text{In}_{0.40}\text{Ga}_{0.60}\text{As}$ QW's, it was found that cropping to 750 pixels x 750 pixels gave the best results.

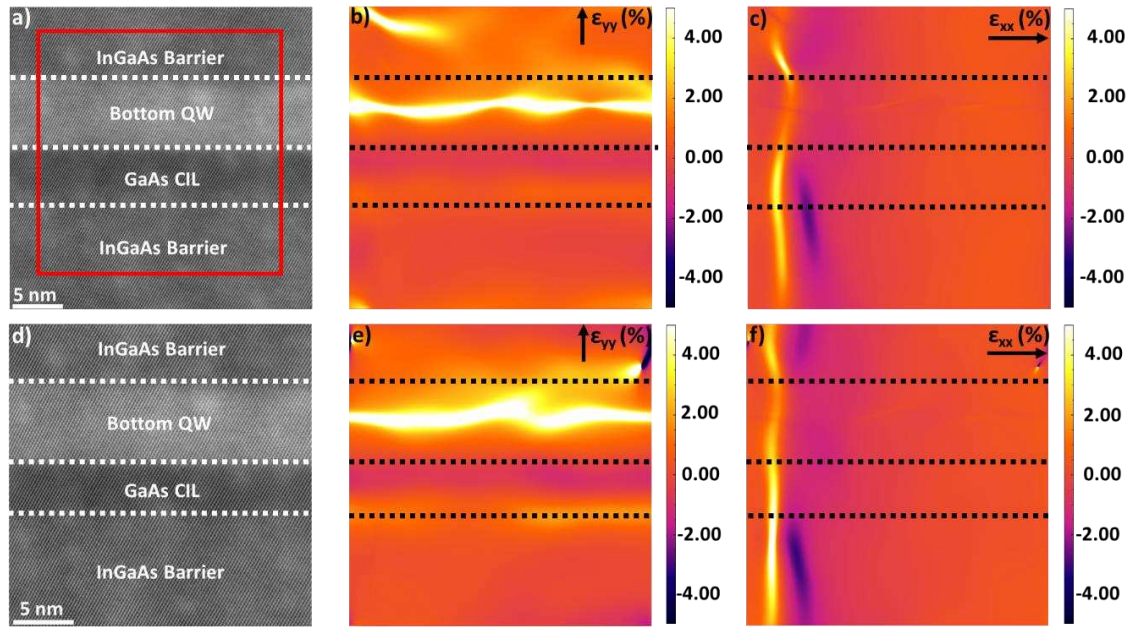


Figure S6. Strain analysis. HAADF-STEM viewed down $[1\ 1\ 0]$ axis images of bottom QW (a,d) with corresponding ϵ_{yy} (b,e) and ϵ_{xx} (c,f) strain maps. Red box in a denotes the cropping region in the 1024×1024 pixels size original image to create the 850×850 pixel size cropped image.

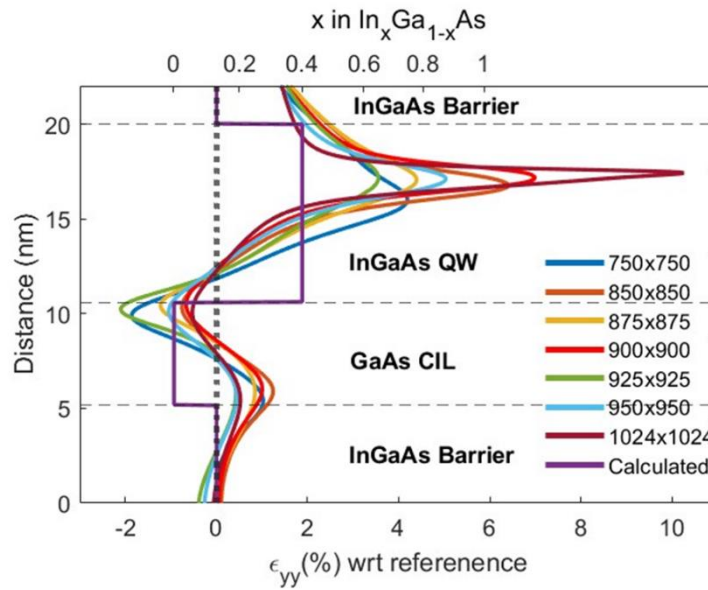


Figure S7. ϵ_{yy} strain line profile for bottom QW under different cropping with number denoting pixel size: 750 pix x 750 pix (blue), 850 pix x 850 pix (orange), 875 pix x 875 pix (gold), 900 pix x 900 pix (red), 925 pix x 925 pix (green), 950 pix x 950 pix (cyan) and 1024 pix x 1024 pix (brown). The calculated ϵ_{yy} (solid purple line in c) is derived using Eq. 2 in the main manuscript and the nominal concentration for each layer.

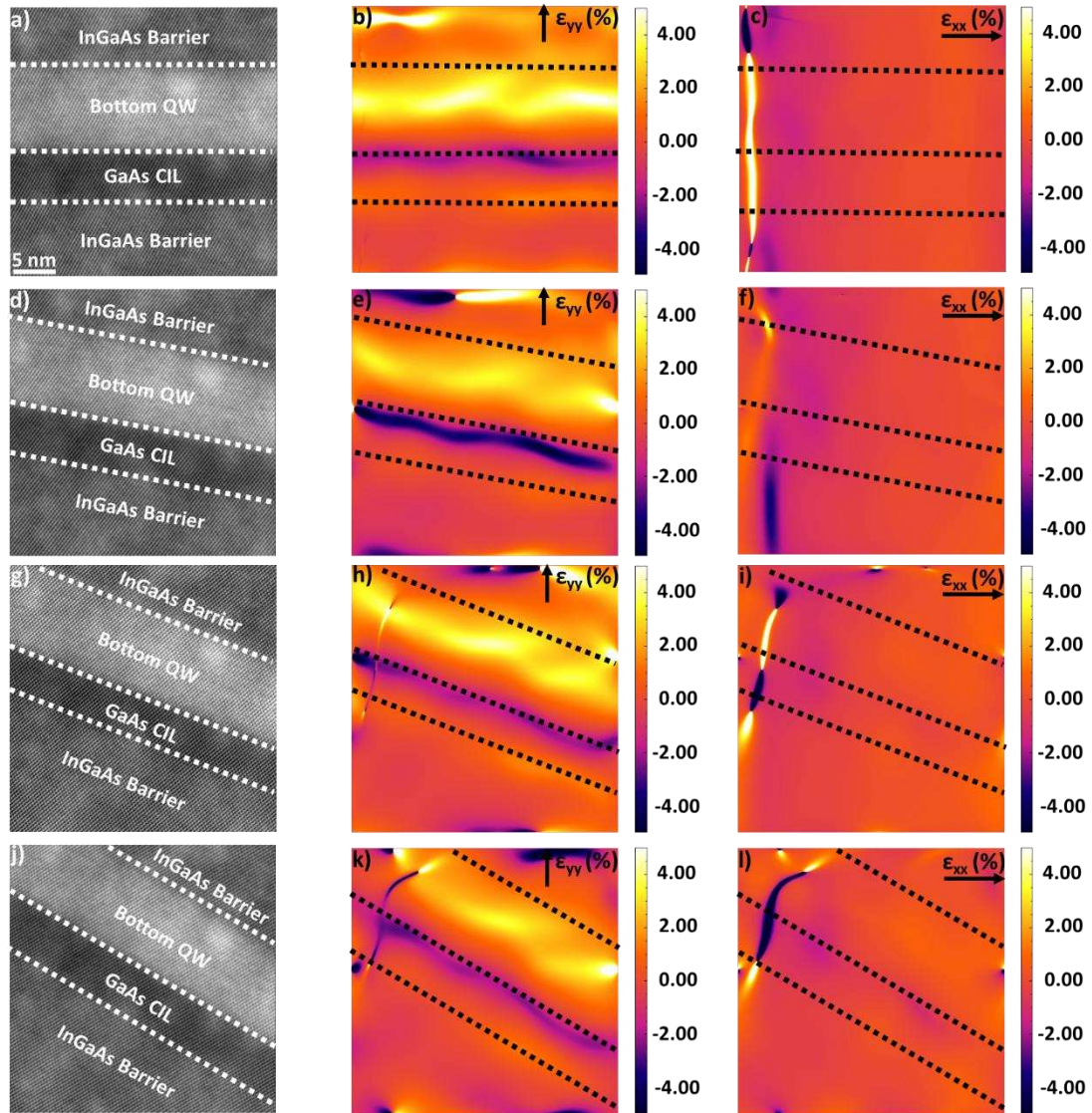


Figure S8. Strain analysis. HAADF-STEM viewed down $[1\ 1\ 0]$ zone axis images for the bottom QW (a,d,g,j) with corresponding ε_{yy} strain map (b,e,h,k) and ε_{xx} strain map (c,f,i,l) under different rotations: no rotation (a-c), 10° (d-f), 20° (g-i) and 30° (j-l). All images cropped to pixel size 750×750 .

Tuning our attention to rotation, it was observed that rotating the HAADF-STEM image clockwise would decrease the intensity of the peaks as observed in Fig. S9. However, it was found that for the other QW's, the rotation would not improve the reduction in the peak intensity significantly.

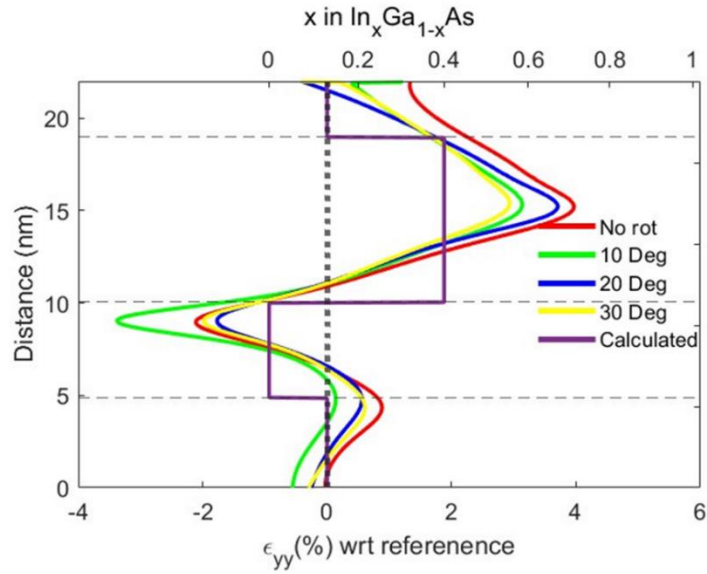


Figure S9. ϵ_{yy} strain line profile for bottom QW under different clockwise rotations: no rotation (red), 10° (green), 20° (blue) and 30° (yellow). Data from images cropped to pixel size 750×750 . The calculated ϵ_{yy} is derived using Eq. 1 and the nominal concentration for each layer.

To ensure consistency and see if there is further potential improvement to the results, analysis using the $\mathbf{g}=\mathbf{2}\bar{2}0$ and $\mathbf{g}=\mathbf{004}$ and corresponding Bright Field (BF)-STEM images was conducted. While the use of $\mathbf{g}=\mathbf{2}\bar{2}0$ and $\mathbf{g}=\mathbf{004}$ vectors for GPA did reduce the strain and showed the strain increasing towards the centre of the QW, the average ϵ_{yy} values from $\mathbf{g}=\mathbf{2}\bar{2}0$ and $\mathbf{g}=\mathbf{002}$ were more sensible. Similarly, BF-STEM images showed that strain was generally highest in the centre of the QW, matching the trends seen in the HAADF images albeit values that such as tensile strain in the QW that were not considered reasonable. After all checks, it was decided that the images used for the main analysis would be the HAADF images cropped to 750×750 pixels with no rotation. The ϵ_{yy} plots for the results used in the main manuscript is shown in Fig S10.

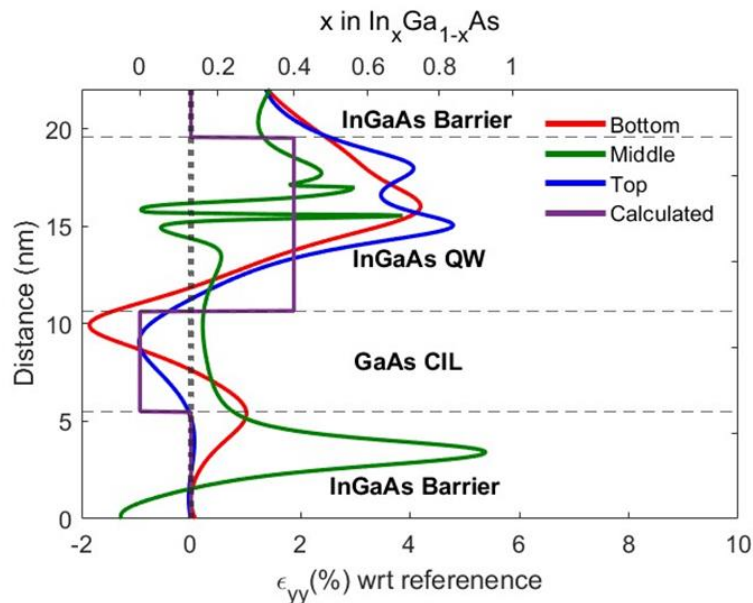


Figure S10. ϵ_{yy} strain line profile for all QWs: bottom (red), middle (green) and top QW (blue). The calculated ϵ_{yy} (solid purple line in c) is derived using Eq. 1 in the main manuscript and the nominal concentration for each layer.

Bandgap measurements

After obtaining the raw electron energy low spectroscopy (EELS) spectra, the initial procedure involves aligning the spectra to ensure the zero-loss peak (ZLP) is precisely at 0eV. This alignment was carried out by using the "align peak" function in Digital Micrograph (DM). Examination of the ZLP (Fig. S11) post-alignment indicated that all peaks were within 0.005eV of 0eV. Considering that the resolution of the monochromator is 0.005eV, it was determined that the ZLP had been successfully aligned.

After alignment, the spectra were denoised using Principal Component Analysis (PCA) in DM. PCA determines the number of significant components present in the spectra via a scree plot, which depicts eigenvalues as function of components. The optimal number of components was determined when the eigenvalues showed minimal change *i.e.* the curve levels off. Based on the scree plots, it was consistently observed that the optimal number of significant components was 10.

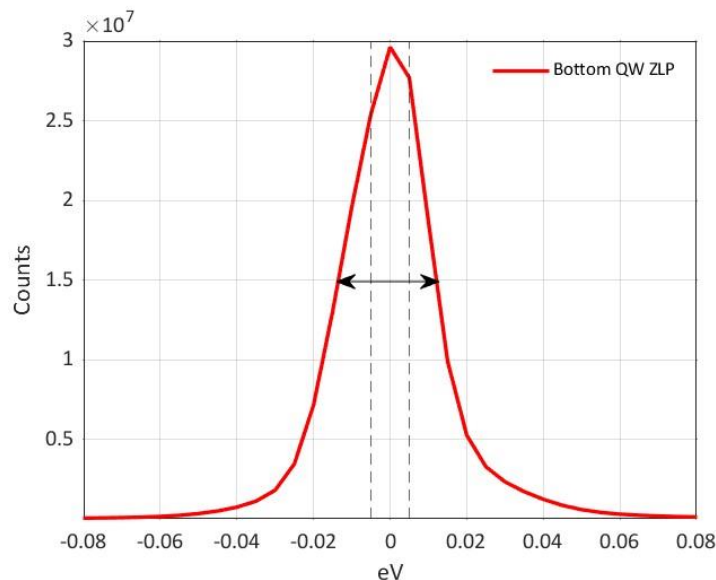


Figure S11. Aligned Raw EELS spectra from the bottom QW. Black dotted line denotes -0.005eV and 0.005eV . Black double head arrow represents the Full Width Half Maxima (FWHM) for the spectra.

Due the presence of parasitic signal in the low loss, such as Cerenkov radiation, simulations are required to extract this noise in order to accurately calculate the E_g . These simulations are based on classical electrodynamics, with the materials described by their frequency-dependent, local dielectric functions. The energy-loss probability is directly separated as the sum of a bulk contribution, which is independent of geometry and proportional to the path length traveled inside each material, and a surface term determined by the interface morphology. In these samples, the surface term is negligible due to the dielectric proximity of the different interfaces, so will only consider the bulk contribution. Both retarded (Γ_{Bulk}^R) and non-retarded (Γ_{Bulk}^{NR}) (*i.e.* assuming an infinite speed of light) calculations were performed and compare them to assess the role of Cerenkov radiation emitted by the fast electrons in their interaction with the bulk materials and, as expected, this affect considerably in the region were we have to fit the E_g . Based on the information provided by the simulated retarded and non-retarded spectral images, we correct the experimental data by subtracting parasitic contributions associated with Cerenkov radiation. The correction function (F_{corr}) is the ratio between the non-retarded bulk loss and the retarded loss (Eq. S3). This function allows to transform the experimental spectrum image (x) to the corrected spectrum image ($F_{corr}(x)$) [2].

$$F_{corr}(x) = \frac{\Gamma_{Bulk}^{NR}}{\Gamma_{Bulk}^R} \cdot x \quad (\text{Eq S3})$$

After that, we perform an automated bandgap fitting in this corrected spectrum. To achieve this, a fitting algorithm evaluates, for each global spectrum, all possible energy ranges within a specified range centered at the reported bulk E_g value of the material. This adaptive range analysis is employed to make the computational cost manageable and to minimise the occurrence of outliers. A goodness-of-fit analysis is then conducted to determine the optimal spectral position at which these characteristic E_g energy patterns are located. Given the properties of the dataset and the data analysis, the statistical parameter used for this analysis is the coefficient of determination (r^2). In each spectrum, we identify the energy range where the fitting yields the highest r^2 value and we utilise this fitting for calculate the E_g value. The error provided for each E_g is the uncertainty from the fitting procedure.

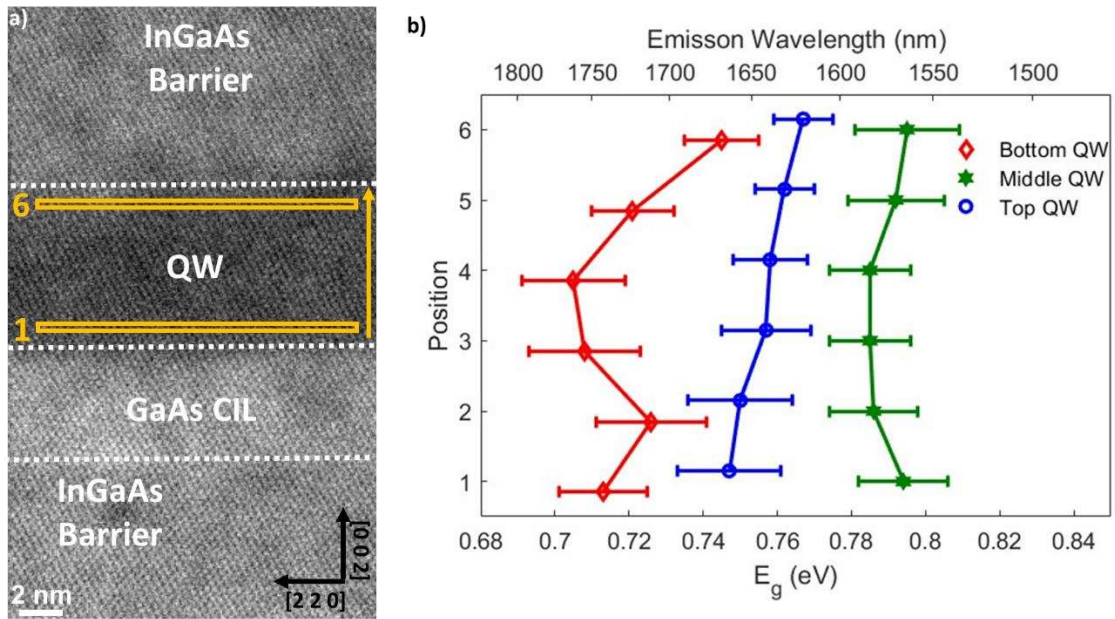


Figure S12. E_g analysis. Representative HAADF-STEM images of the middle QW (a), and the corresponding measured E_g uncorrected for Cerenkov (b): bottom (red diamond), middle (green hexagon) and top QW (blue circle). The E_g was measured horizontally as indicated by the yellow marking in a). The secondary axis indicates the corresponding emission wavelength.

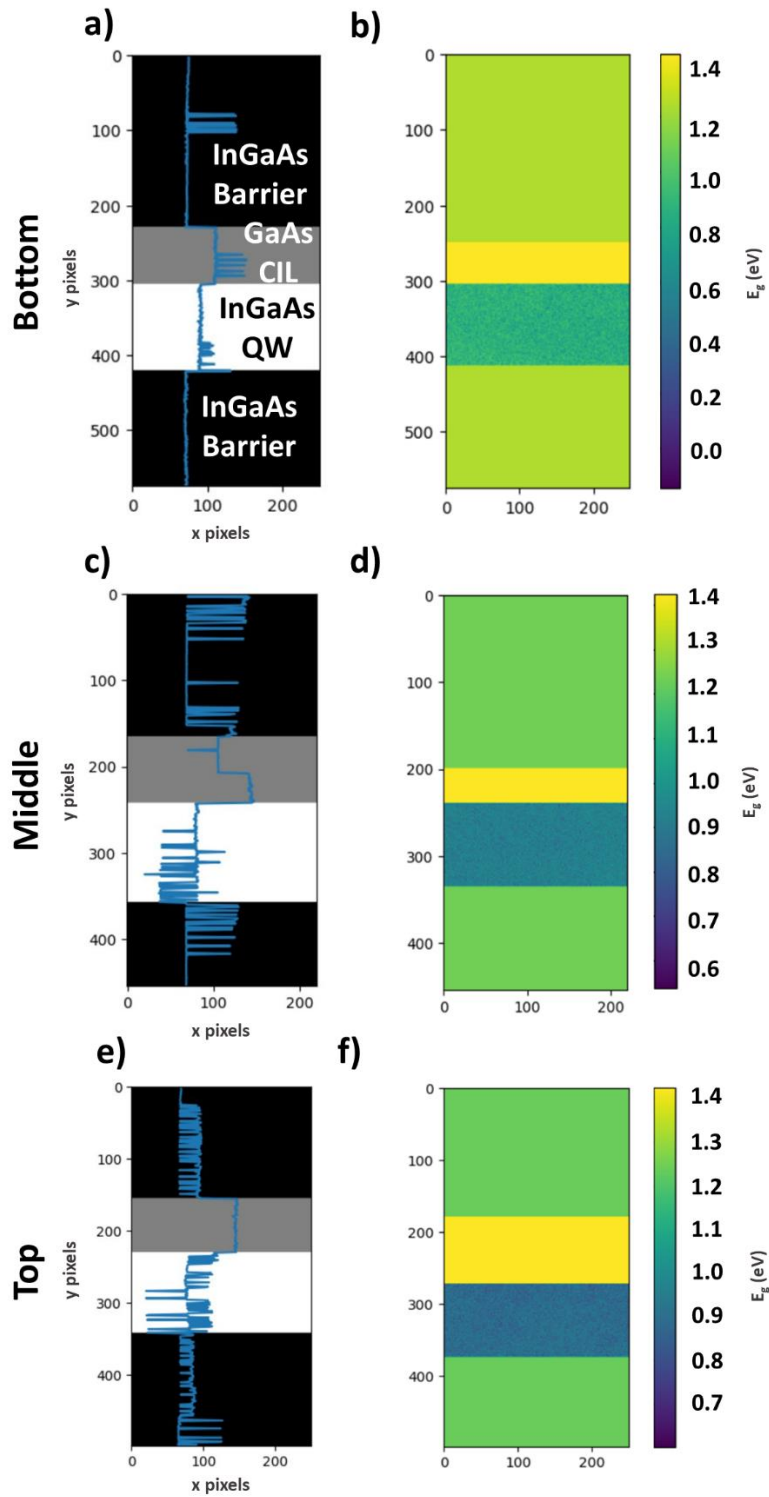
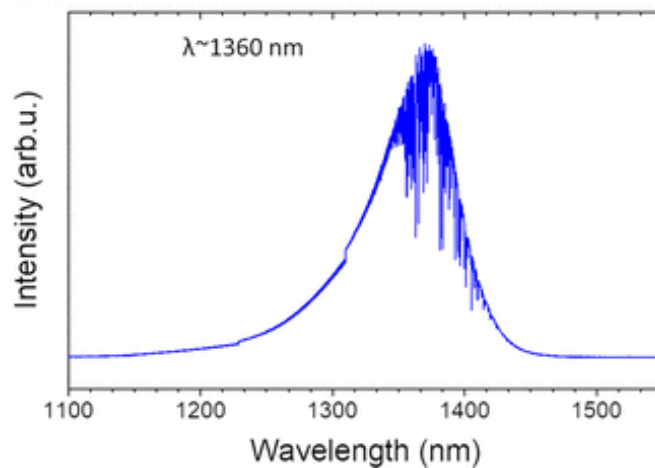


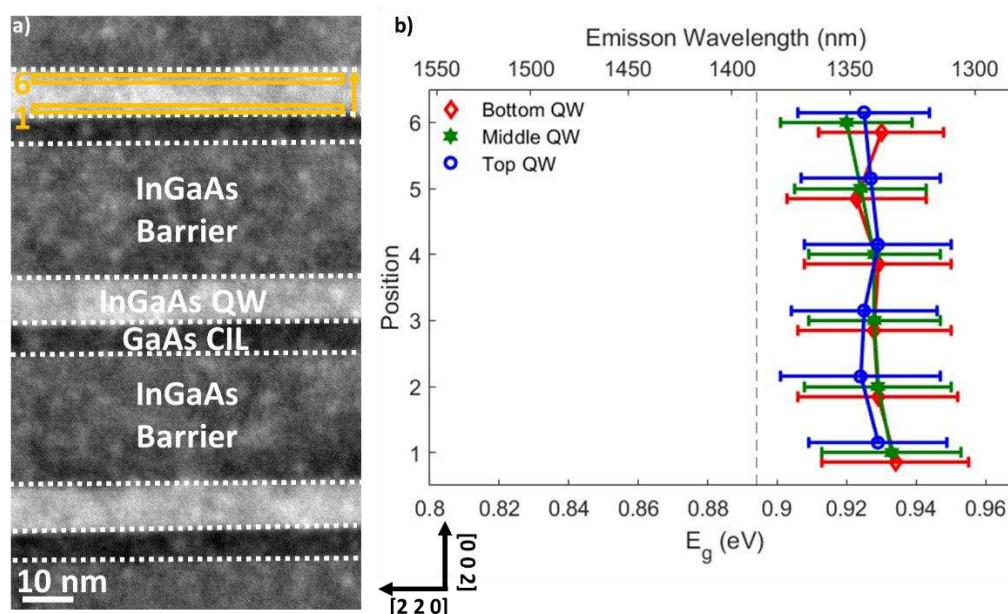
Figure S13. E_g variations across neighbouring layers (b,d,f) for bottom and top (e,f) QW.



variations across (a,c,e) and E_g map (a,b), middle (c,d)

Figure S14. Photoluminescence spectra of QWs. From [1].

Figure S15 shows the E_g analysis for all of the QW's in the EELS acquisition which has a lower spatial resolution compared to the individual file for the QW used in the main manuscript. We observe that there is no significant E_g variation between the position within each QW and as an average over all of the QW's. This could be due the similarities in the ZLP for each QW EELS spectra which were all nearly identical, likely because of the lower spatial resolution, that would consequently carry over when processed to calculate E_g . Overall, these results highlight the of the importance and motive for



using individual QW EELS spectra with higher pixel resolution to resolve the E_g of the QWs.

Figure S15. E_g analysis. Representative HAADF-STEM images over all 3 QW's (a), and the corresponding measured E_g corrected for Cerenkov (b): bottom (red diamond), middle (green hexagon) and top QW (blue circle). The E_g was measured horizontally as indicated by the yellow markings for the top QW in a). The secondary axis indicates the corresponding emission wavelength.

Potential lamella thickness effects were investigated by measuring the relative thickness (t/λ) across the QWs for the sample used for low loss EELS. This was done using the relative thickness function in Digital Micrograph across all three QWs and then taking the t/λ value at each position as shown in Fig. S16. The bottom QW is the thinnest and the top QW is the thickest area, ranging from ~ 0.42 to $0.52 t/\lambda$. A common feature is that the thickness increases at the centre of each QW. Upon examining the E_g measurements, it was determined that the difference in lamella thickness is not large enough to affect the measurements.

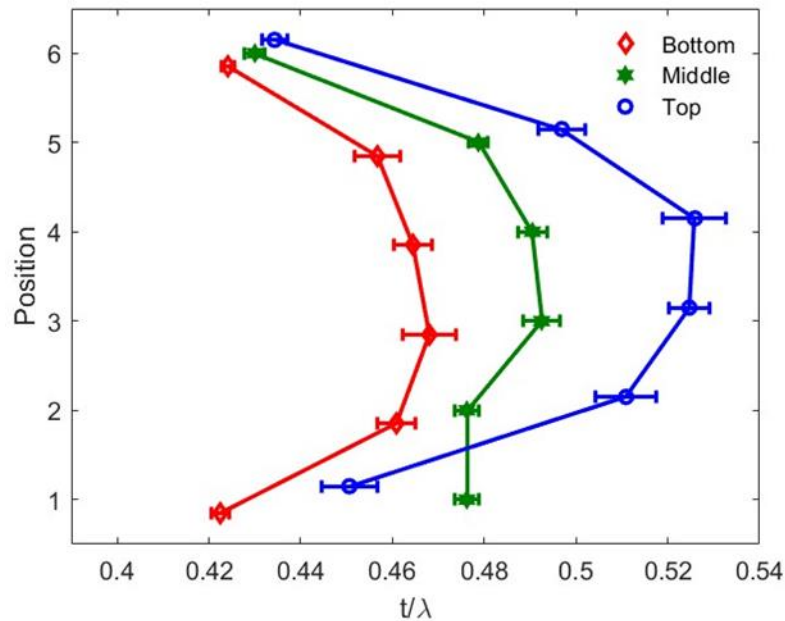


Figure S16. Relative thickness (t/λ) plot at each position for the bottom (red diamond), middle (green hexagon) and top (blue circle) $In_{0.40}Ga_{0.60}As$ QW.

The Cerenkov corrected E_g and measured In concentration for the middle and top QW are presented in Figure S17. For all QW, positions 2-5 compare well with the optical E_g with the E_g at position 1 (the GaAs CIL interface) is significantly lower. For position 6 (the $In_{0.13}Ga_{0.87}As$ barrier interface) in the top QW, the measured E_g is significantly lower compared to the optical E_g as was seen in the bottom QW. In contrast, the E_g for the middle QW is within the optical E_g after considering uncertainty. The values and uncertainties for both x in $In_xGa_{1-x}As$ and the E_g in Fig. S17 are presented in Table S5.

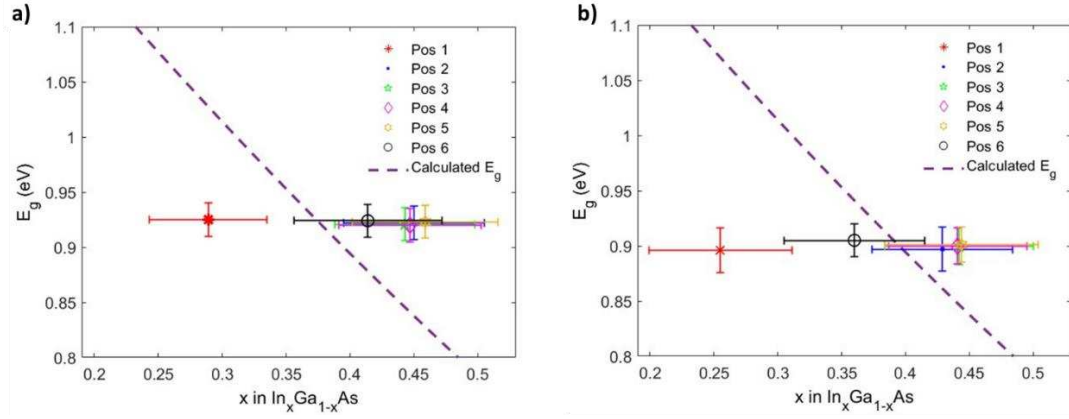


Figure S17. Comparison of the calculated and measured Cerenkov corrected E_g values at each position (1-6) for the middle (a) and top QW (b) as function of In mole fraction (x). The calculated E_g as a function of x (dotted purple line) based on Eq. 2 from Nahroy et al.[3].

QW	Position	Non-Corrected E_g (eV)	Corrected E_g (eV)	x in $\text{In}_x\text{Ga}_{1-x}\text{As}$
Bottom	1	0.713±0.012	0.881±0.019	0.316±0.058
	2	0.726±0.015	0.866±0.022	0.433±0.058
	3	0.708±0.015	0.877±0.022	0.433±0.055
	4	0.705±0.014	0.875±0.021	0.437±0.051
	5	0.721±0.011	0.884±0.018	0.440±0.060
	6	0.745±0.010	0.897±0.018	0.339±0.054
	Average	0.720±0.012	0.883±0.020	0.395±0.081
Middle	1	0.794±0.012	0.925±0.016	0.274±0.044
	2	0.786±0.012	0.921±0.016	0.439±0.055
	3	0.785±0.011	0.920±0.016	0.460±0.056
	4	0.785±0.011	0.919±0.017	0.468±0.055
	5	0.792±0.013	0.924±0.017	0.462±0.058
	6	0.795±0.014	0.926±0.016	0.422±0.056
	Average	0.790±0.012	0.922±0.016	0.419±0.083
Top	1	0.747±0.014	0.898±0.020	0.262±0.054
	2	0.750±0.014	0.900±0.019	0.417±0.054
	3	0.757±0.012	0.905±0.017	0.428±0.056
	4	0.758±0.010	0.906±0.016	0.439±0.049
	5	0.762±0.008	0.908±0.014	0.448±0.061
	6	0.767±0.008	0.911±0.014	0.355±0.054
	Average	0.757±0.011	0.905±0.017	0.393±0.081

Table S5. Measured non-corrected and Cerenkov corrected E_g and x in $\text{In}_x\text{Ga}_{1-x}\text{As}$ at each position for each $\text{In}_{0.40}\text{Ga}_{0.60}\text{As}$ QW.

Comparison of uncorrected Cerenkov E_g not corrected for Cerenkov and measured In concentration (Fig. S18) show that even with the inclusion of uncertainty, the measured E_g and In atomic fraction does not fall within the optical E_g from Nahory [3]. This further validates the importance of correcting the Cerenkov radiation effects to ensure an accurate E_g measurement.

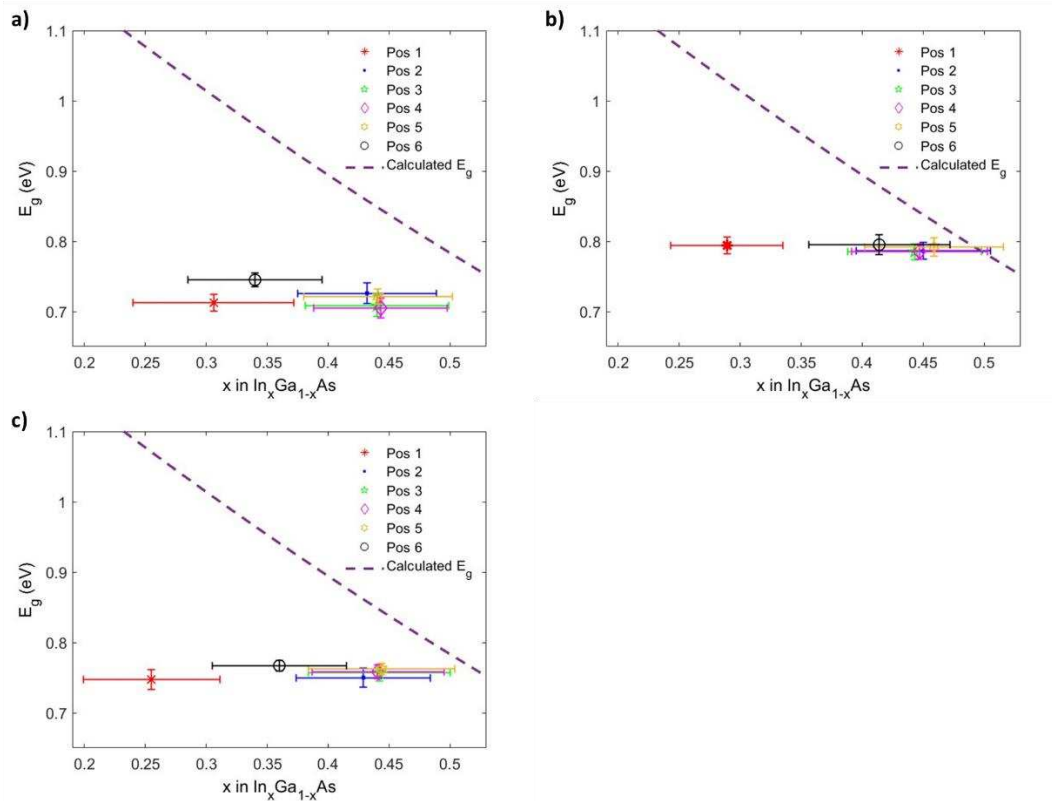


Figure S18. Comparison of the calculated E_g and measured non-Cerenkov corrected E_g values at each position (1-6) in the bottom (a), middle (b) and top QW (c) as function of In mole fraction (x). The calculated E_g as a function of x (dotted purple line) based on Eq. 2 from Nahory et al. [3].

Figure S19 presents the simulated EELS for the outlined concentrations measured. The onset energy from each of the simulated EELS of $\text{In}_x\text{Ga}_{1-x}\text{As}$ alloys were extracted by finding the energy where the loss function is significantly greater than zero *i.e.* above the x-axis. Initial numbers for the loss function were in the magnitude of 10^{-17} which were considered close to zero. It was decided that the $<10^{-5}$ was the smallest number significantly above zero hence the lowest energy with was considered to be the onset energy for Fig. 5c in the main manuscript.

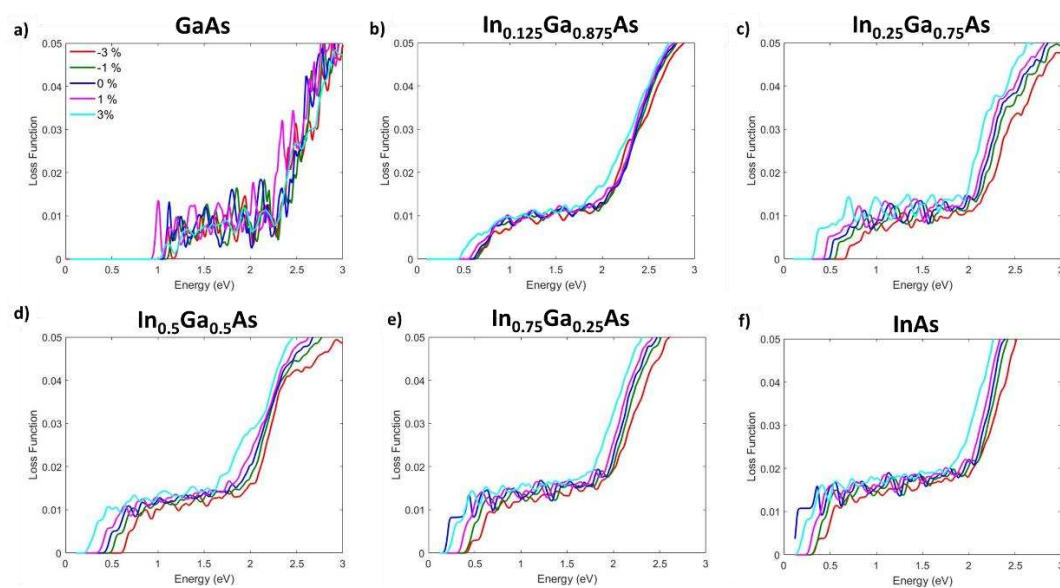


Figure S19. Simulated EELS of GaAs (a), $\text{In}_{0.125}\text{Ga}_{0.875}\text{As}$ (b), $\text{In}_{0.25}\text{Ga}_{0.75}\text{As}$ (c), $\text{In}_{0.50}\text{Ga}_{0.50}\text{As}$ (d), $\text{In}_{0.75}\text{Ga}_{0.25}\text{As}$ (e) and InAs (f). Coloured lines denote the strain in each of the $\text{In}_x\text{Ga}_{1-x}\text{As}$ alloys.

References

1. Mura EE, Gocalinska AM, O'Brien M, et al (2021) Importance of Overcoming MOVPE Surface Evolution Instabilities for $>1.3 \mu\text{m}$ Metamorphic Lasers on GaAs. *Cryst Growth Des* 21:2068–2075. <https://doi.org/10.1021/acs.cgd.0c01498>
2. Martí-Sánchez S, Botifoll M, Oksenberg E, et al (2022) Sub-nanometer mapping of strain-induced band structure variations in planar nanowire core-shell heterostructures. *Nat Commun* 13:4089. <https://doi.org/10.1038/s41467-022-31778-3>
3. Nahory RE, Pollack MA, Johnston WD, Barns RL (1978) Band gap versus composition and demonstration of Vegard's law for $\text{In}_{1-x}\text{Ga}_x\text{As}_y\text{P}_{1-y}$ lattice matched to InP. *Appl Phys Lett* 33:659–661. <https://doi.org/10.1063/1.90455>